OPEN ACCESS Freely available online

PLOS | ONE

Parametric Representation of Multiple White Matter Fascicles from Cube and Sphere Diffusion MRI

Benoit Scherrer*, **Simon K. Warfield**

Computational Radiology Laboratory, Department of Radiology Children's Hospital, Boston, Massachusetts, United States of America

Abstract

The characterization of the complex diffusion signal arising from the brain remains an open problem. Many representations focus on characterizing the global shape of the diffusion profile at each voxel and are limited to the assessment of connectivity. In contrast, Multiple Fascicle Models (MFM) seek to represent the contribution from each white matter fascicle and may be useful in the investigation of both white matter connectivity and diffusion properties of each individual fascicle. However, the most appropriate representation of multiple fascicles remains unclear. In particular, a multiple tensor representation of multiple fascicles has frequently been reported to be numerically challenging and unstable. We provide here the first analytical demonstration that when using a diffusion MRI acquisition with only one non-zero b-value, such as in conventional single-shell HARDI acquisition, a co-linearity in model parameters makes the precise model estimation impossible. Motivated by this theoretical result, we propose the novel CUSP (CUbe and SPhere) optimal acquisition scheme to achieve multiple non-zero b-values. It combines the gradients of a single-shell HARDI with gradients in its enclosing cube, in which varying b-values can be acquired by modulation of the gradient strength, without modifying the minimum echo time. Compared to a multi-shell HARDI acquisition, our scheme has significantly increased signal-to-noise ratio. We propose a novel estimation algorithm that enables efficient, robust and accurate estimation of the parameters of a multi-tensor model. In conjunction with a CUSP acquisition, it enables *full* estimation of the multi-tensor model. We present an evaluation of CUSP-MFM on both synthetic phantoms and invivo data. We report qualitative and quantitative experimental evaluations which demonstrate the ability of CUSP-MFM to characterize multiple fascicles from short duration acquisitions. CUSP-MFM enables rapid and effective investigation of multiple white matter fascicles, in both normal development and in disease and injury, in research and clinical practice.

Citation: Scherrer B, Warfield SK (2012) Parametric Representation of Multiple White Matter Fascicles from Cube and Sphere Diffusion MRI. PLoS ONE 7(11): e48232. doi:10.1371/journal.pone.0048232

Editor: Christopher P. Hess, UCSF, United States of America

Received December 5, 2011; **Accepted** September 28, 2012; **Published** November 26, 2012

Funding: This investigation was supported by National Institutes of Health grants R01 RR021885, R01 EB008015, R03 EB008680, R01 LM010033, R42 MH086984 and UL1 RR025758. The funders had no role in study design, data collection and analysis, decision to publish, or preparation of the manuscript.

Competing Interests: The authors have declared that no competing interests exist.

* E-mail: benoit.scherrer@childrens.harvard.edu

Introduction

Measuring water diffusion with magnetic resonance diffusion weighted imaging (MR-DWI) has enabled non-invasive investigation and characterization of the white matter architecture and microstructure in the brain. The diffusion in a white matter fascicle has been observed to be highly anisotropic, with primary orientation corresponding to the orientation of the fascicle [1,2]. The underlying microstructure that gives rise to this anisotropy has been reviewed recently by [3–5]. Diffusion tensor imaging (DTI) [6] was proposed to describe the three-dimensional nature of anisotropic diffusion. Assuming *homogeneous Gaussian diffusion* within each voxel, DTI describes the magnitude and orientation of water molecule diffusion with a second-order tensor estimated from diffusion measurements in several directions. More precisely, DTI relates the measured diffusion-weighted signal S_k along a gradient direction $\mathbf{g}_k$ to the non-attenuated signal S_0 via the Stejskal-Tanner equation [7]:

$$S_k(\mathbf{D}) = S_0 e^{-\mathrm{TE}/\mathrm{T2}} e^{-\gamma^2\delta^2(\Delta-\delta/3)\mathbf{g}_k{}^T\mathbf{D}\mathbf{g}_k}, \tag{1}$$

where TE is the echo time, T2 the spin-spin (or transverse) relaxation time of the tissue, γ the gyromagnetic ratio, δ and Δ the diffusion sensitizing pulse gradients duration and time separation, and $\mathbf{D}$ is the 3×3 diffusion tensor. The applied b-value defined by $b_k = \gamma^2\delta^2(\Delta-\delta/3)G_k^2$, which depends on the gradient strength $G_k^2 = \|g_k\|^2$, has been introduced [8] to simplify the notations in Eq. 1 and describes the diffusion sensitization strength. The nominal b-value $b_{\mathrm{nominal}} = \gamma^2\delta^2(\Delta-\delta/3)$ describes the b-value for the unit-norm gradients. The term $e^{-\mathrm{TE}/\mathrm{T2}}$ is generally considered constant across all gradients and omitted. However, and importantly, it highlights how the signal amplitude $S_k(\mathbf{D})$ decreases exponentially for increasing TE. A larger TE considerably alters the signal-to-noise ratio for *all* the measurements (see Fig. 1), regardless of the applied b-value. This is essential because minimum achievable TE and nominal b-value are linked. They follow a complex relationship [9,10] via the timing parameters δ and Δ, which can be approximated by $\mathrm{TE} \approx \left(\frac{12 b_{\mathrm{nominal}}}{\gamma^2}\right)^{1/3}$ [11,12]. Consequently, increasing the nominal b-value increases the minimum achievable TE, which in turn leads to an exponentially decreased signal amplitude closer to the noise floor (see Fig. 1). Considering that the noise amplitude is constant, this signal dropout leads to a lower SNR for each DW image, regardless of their b-value [13]. This leads to a fundamental trade-off in diffusion imaging: while higher b-values are

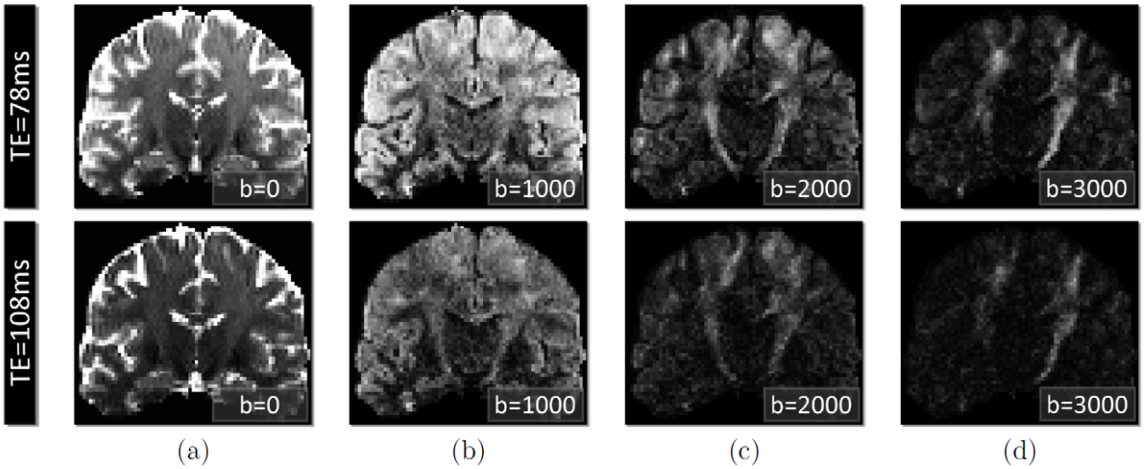

Figure 1. Illustration of the signal decrease when the echo time and the b-value increase in DWI. Diffusion-weighted acquisition with $b=0s/mm^2$ (a), $b=1000s/mm^2$ (b), $b=2000s/mm^2$ (c) and $b=3000s/mm^2$ (d). Comparison for $\mathrm{TE}=78\mathrm{ms}$ (first line) obtained when using our CUSP sequence with $b\leq 3000s/mm^2$, and $\mathrm{TE}=108\mathrm{ms}$ (second line) obtained when using multi-shell HARDI sequence with $b\leq 3000s/mm^2$. It shows how the signal amplitude decreases (and so does the signal-to-noise ratio) when the b-value *and the TE* increase (first line versus second line). Acquisitions with a short TE should be favored, particularly when imaging at high b-value.
doi:10.1371/journal.pone.0048232.g001

known to increase the contrast *between* the DW gradient directions [14], and therefore to increase the reliability of estimation of orientation of each fascicle, the higher nominal b-value also leads to a longer TE and to a lower SNR *for each DW image*, decreasing the estimation certainty and quality. An optimal diffusion-weighted acquisition must achieve a trade-off between acquiring adequate b-values while minimizing the TE to maximize the SNR.

DTI and its underlying mono-exponential signal attenuation assumption are generally considered to satisfactorily represent *single* fascicles when imaging with b-values lower than $3000s/mm^2$ [15–17], which is frequently the case in clinical settings. Non-monoexponential behavior of the signal at a voxel in this b-value range can arise from CSF partial voluming [18], mixtures of fascicles present in the voxel [19] and other sources [4]. The diffusion tensor enables representation of the orientation of a single fascicle as well as the characterization of the diffusion process. Tensor parameters such as the fractional anisotropy (FA), the mean diffusivity (MD), the axial diffusivity (AD) and the radial diffusivity (RD) can be computed and have been shown to provide valuable information that reflects changes in the white matter due to development, disease and degeneration. DTI requires relatively short acquisition times and has been successfully employed in clinical studies.

DTI is however well known to be a poor parametric model for representing the diffusion signal arising at voxels that encompass multiple fascicles with heterogeneous orientation such as fascicle crossing, kissing or fanning. A wide number of approaches have been investigated to overcome this fundamental limitation. They involve both novel *diffusion signal sampling schemes* and novel *ways to analyze the diffusion signal* as detailed below.

Image acquisition strategies

Mainly two q-space sampling strategies have been used for complex fiber structure assessment: Cartesian sampling and spherical sampling. Cartesian sampling is used by diffusion spectrum imaging (DSI) [20,21]. However, it requires an extremely high number N of measurements, typically $200\leq N\leq 512$, preventing the technique from being used in routine clinical practice. Spherical sampling as employed in high angular resolution imaging (HARDI) techniques reduces the imaging time and requires moderate imaging gradients intensity. A large number of HARDI-based techniques have been proposed (see next section). Note that in this work, to avoid any confusion between the image acquisition strategy and the signal modeling strategy, we denote by HARDI the *acquisition scheme* only. Single-shell HARDI acquisitions with a single non-zero b-value have been considered to image a sphere of constant radius in q-space. Multiple-shell HARDI acquisitions have also been proposed. They combine in a single acquisition the sampling of multiple shells of different radius in q-space. It enables acquisition of multiple non-zero b-values. Multiple-shell HARDI, however, leads to a large TE that depends upon the highest b-value. This leads in turn to a significantly lower signal-to-noise ratio (SNR) for all the measurements (see Eq. 1 and [22]) and to a longer imaging time. In addition, imaging a higher b-value is generally achieved by using longer diffusion gradient pulse duration, which in turn leads to larger eddy current distortion [23,24].

Other sampling techniques have been proposed for reasons other than assessing complex fiber structures. Sampling using the tetrahedral $\sqrt{3}$-norm gradients has been employed [9] to measure the apparent diffusion coefficient (ADC) from four diffusion measurements. Because $b_k=b_{\mathrm{nominal}}G_k^2$, it enables imaging at higher b-value than the nominal b-value *without* modifying the timing parameters δ and Δ, but by using *gradients with norm greater than one*. It provides the optimal minimum achievable TE for the corresponding applied b-value, leading to a better SNR and potentially to lower eddy current distortion because the diffusion gradient pulses can be shortened. Using the same concept [25], employed the six hexahedral $\sqrt{2}$-norm gradients to estimate a diffusion tensor from seven measurements. Furthermore, in CURVE-Ball (CUbe Rays to Vertices and Edges) [26], a spherical sampling and the hexahedral [25] and tetrahedral [9] gradients were combined to perform the estimation of a single-tensor model at three different diffusion scales b_{nominal}, $2b_{\mathrm{nominal}}$ and $3b_{\mathrm{nominal}}$.

Models for characterization of the diffusion signal

A large number of approaches have been investigated to analyze the diffusion signal and represent multiple white-matter fascicles with complex geometry. Both parametric (model-based) and non-parametric (model-free) approaches have been proposed. They generally focus on estimating either (1) the diffusion displacement probability density function (diffusion PDF), (2) the diffusion orientation distribution function (dODF) which is the angular profile of the diffusion PDF or (3) the fiber orientation distribution function (fODF), also known as the fiber orientation density (FOD) and which is of central interest for tractography.

Model-free approaches include diffusion spectrum imaging (DSI) [20,21]. In this technique, the diffusion PDF is directly estimated from the inverse Fourier transform of the measured signal, requiring a very high number of measurements to satisfy the Nyquist condition. Q-ball imaging (QBI) [27] estimates an approximate non-parametric angular profile of the diffusion PDF without actually computing the diffusion PDF, by using the Funk-Radon transform. Fast and robust analytical QBI estimation procedures have been proposed [28–31]. However, QBI results in the estimation of an approximated dODF related to the true dODF by modulation with a zero-order Bessel function. This leads to a spectral broadening of the diffusion peaks of individual fascicles at moderate b-values accessible on a clinical scanner, perturbing the FOD reconstruction necessary for carrying out tractography. Mixing of individual tracts in a voxel leads to local maxima that do not coincide with the true fascicle orientation [32], leading to a relatively low fidelity representation. To avoid the usual Q-Ball approximation, Canales-Rodríguez *et al.* [33] have derived in Exact Q-Ball Imaging (EQBI) a direct relationship between the dODF and the diffusion data. Its enables the estimation of the exact dODF under the assumption of a Gaussian profile.

Q-space approaches such as DSI, QBI, or EQBI are however limited by three major error sources. First they are based on the *narrow pulse approximation* assumption, considering that molecules do not diffuse during the application of the diffusion sensitizing gradients. The gradient pulses are then modeled by a Dirac shape which is not practically feasible, especially on clinical systems. In practice, in clinical settings, the diffusion-encoding gradient duration δ is typically of the same order of magnitude as the time offset Δ between encoding gradients [34] ($\Delta/\delta \approx 1$) to minimize T_2 decay and to obtain better SNR, which is a very poor approximation of a Dirac shape. Second, since the imaging time has to be finite, only a finite region in q-space is imaged. This has been shown to lead to a blurred propagator with decreased contrast and angular resolution [35]. Third, they are limited by the need to truncate the Fourier representation which is required to numerically compute the infinite series involved in the Fourier transformation, leading to quantization artifacts [33].

In contrast, parametric models describe a predetermined model of diffusion rather than an arbitrary one. They potentially require a smaller number of images to be acquired, leading to a reduced acquisition time. A large number of model-based approaches have been investigated. Among them, generalized diffusion tensor imaging (GDTI) [36,37] models the white-matter fascicles with higher-order tensors ; spherical deconvolution (SD) [38–40] directly estimates the FOD instead of the dODF and has a better angular resolution; diffusion orientation transform (DOT) [16] employs a model-based q-space modeling based on the assumption of a monoexponential decay of the signal attenuation.

A major drawback to DSI, QBI, DOT, SD and GDTI is that they focus on describing the *general shape* of the diffusion profile in each voxel. They do not represent each fascicle independently and therefore do not characterize the proportion of each fascicle passing through a voxel. Importantly, they do not enable characterization of each fascicle. Diffusion parameters such as the generalized fractional anisotropy (GFA) can be computed but represent a DW signal dispersion property rather than an individual fascicle property. For example, a synthetic fascicle consisting of an identical tensor at every voxel crossed by another synthetic fascicle has a GFA that varies in the crossing region [41], which is not clinically relevant. It is not possible to distinguish whether a change in diffusion parameters along a fascicle is associated with a change in the intrinsic fascicle property or because of the presence of crossing fascicles. These approaches provide information about the distribution of fascicle *orientations* in the voxel but are limited to connectivity assessment.

In contrast, multi-fascicle models (MFM) consider at each voxel a mixture of independent fascicles with heterogeneous orientation. Making the assumption of a slow exchange between the fascicles' compartments, the diffusion signal in each voxel is modeled as a mixture of the diffusion signal arising from each individual fascicle. Integration of an isotropic component has also been investigated [17,42–45] to model the diffusion of unrestricted water. This enables characterization of pathologies such as edema, stroke or inflammation. This also enables characterization of the CSF contamination [46] due to partial volume effect, known to perturb the accurate estimation of the anisotropic diffusion compartments [18,47]. Ultimately, the diffusion-weighted signal S_k along a gradient direction $\mathbf{g}_k$ for MFM with an isotropic compartment and N_f fascicles can be described by the following general mixture:

$$S_k(\mathbf{D},\mathbf{f}) = S_0(f_0 S_k^{\text{free\_water}} + \sum_{j=1}^{N_f} f_j S_{k,j}^{\text{single\_fascicle}}), \qquad (2)$$

where $S_{k,j}^{\text{single\_fascicle}}$ is the diffusion signal arising from a single fascicle, $S_k^{\text{free\_water}}$ is the diffusion signal arising from the unrestricted water diffusion, and $\mathbf{f} = (\mathbf{f}_0, \ldots, \mathbf{f}_{N_f})$ describes the *fractions of occupancy* of each compartment ($f_j \in [0,1]$) and sum to one.

The diffusivity of free water is generally considered to be well modeled by an isotropic Gaussian distribution [17,42–45], leading to $S_k^{\text{free\_water}} = e^{-b_k D_{\text{iso}}}$ with D_{iso} is the diffusivity of free water.

In a particular case of multi-fascicle model, the ball-and-stick model [42,43], each individual fascicle has been represented by a stick in the expression of $S_{k,j}^{\text{single\_fascicle}}$. With this simplification, an essential advantage of multi-fascicle models is lost: the ball-and-stick model provides information only about the fascicles orientation. It does not enable the assessment of fascicle properties such as the fascicle anisotropy and diffusivity, limiting the use of the ball-and-stick model to connectivity studies.

In contrast, since an individual fascicle is generally considered to be well represented by a single tensor in DTI, a natural candidate has been to represent each fascicle by a tensor. Considering N_f tensors $\mathbf{D} = (\mathbf{D}_1, \ldots, \mathbf{D}_{N_f})$ representing the N_f fascicles, this amounts to setting $S_{k,j}^{\text{single\_fascicle}} = e^{-b_k \mathbf{g}_k{}^T \mathbf{D}_j \mathbf{g}_k}$, leading to the so-called multi-tensor model [42,45,48–52]. The multi-tensor model has the fundamental advantage over other common representations of modeling each fascicle independently. It enables the assessment of *individual* fascicle characteristics by computing diffusion tensor parameters for each fascicle. This enables characterization of the white-matter appearance, changes and alterations. This also enables comparison of diffusion characteristics between corresponding anatomical fascicles across individuals, which is of great interest for clinical applications. In addition, the *full* multi-tensor model estimation enables characterization of the fraction of occupancy for *each* fascicle, providing information about the mixing proportions and compensating for partial volume effect.

Multiple works have pointed out that a non-monoexponential decay may be observed *in voxels* when imaging with high b-values [3–5,15,6,53–59], providing evidence that the *single tensor model* and its underlying Gaussian assumption is not appropriate to accurately represent the diffusion signal *in the voxel*. The biophysical mechanisms responsible for the non-monoexponential behavior are, however, numerous and not completely understood. First, it is commonly recognized that compartmentalization of the voxel in different subregions with heterogeneous properties can lead to a non-monoexponential decay [3,4,56] under certain acquisition conditions. Particularly, as illustrated by Fig. 2, mixing of an isotropic unrestricted water compartment with multiple anisotropic compartments (Equation 2), each of them being modeled with a purely monoexponential decay, leads to a non-monoexponential decay due to partial volume averaging, even at moderate b-values. At a smaller diffusion scale, the presense of intra- and extracellular compartments does lead to a non-monoexponential decay for very high b-values, even for a single fascicle. Nevertheless, the presence of this phenomenon at clinically relevant b-values, with long diffusion sensitization pulse duration δ, long echo times and low signal-to-noise ratio remains unclear.

Importantly, compartmentalization is not a prerequisite for the presence of a non-monoexponential decay. Schwarcz *et al.* [57] have reported the presence of a biexponential decay in the cold-injured brain parenchyma *after massive membrane disintegration*, and in centrifuged erythrocyte samples. Sehy *et al.* [54] have observed non-monoexponential behavior within the intracellular space of a *single* cell, the frog oocyte. Other biophysical mechanisms, such as the proximity of cell membranes which locally restrict motion, and intra- and inter-cellular heterogeneities, are likely to contribute to the MR signal decay behavior. Imaging strategies that uniquely characterize each of these properties remain under development [3–5,56].

Multiple approaches have been investigated to account for the non-Gaussianity of the diffusion signal in a voxel [5], including fitting a multi-exponential model [4,16,53,58] and a "stretched-exponential model" [55]. Jensen *et al.* [59] have investigated the estimation of a Kurtosis term, which is a dimensionless measure of the deviation of the water diffusion profile from a Gaussian distribution. Assaf *et al.* [15] proposed a 'composite hindered and restricted model of diffusion' (CHARMED), in which the diffusion signal was characterized by components arising from hindered (extra-axonal water) and restricted (intra-axonal) water diffusion, featuring a perpendicular diffusion component that is non-monoexponential. CHARMED requires long acquisition times and very high b-values (up to $10000\text{s}/\text{mm}^2$), limiting its use in routine clinical practice.

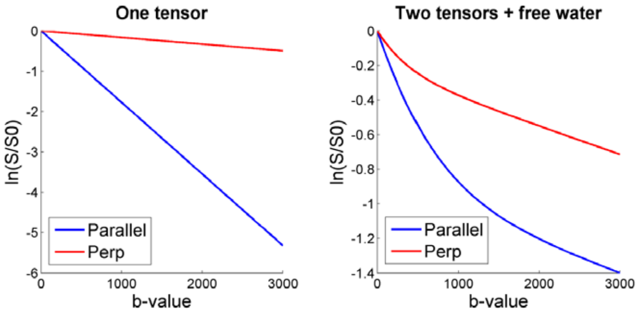

(a) (b)

Figure 2. Intra-voxel orientation heterogeniety and partial volume averaging leads to a non-monoexponential decay in a voxel. (a): Illustration of the monoexponential decay arising from a single tensor (FA $=0.9$, diffusivity $=2.1\times10^{-3}\text{mm}^2/\text{s}$) as shown by the linearity of $\log(S/S_0)$ in both the parallel and perpendicular directions with respect to the tensor orientation (noise-free case). (b): Illustration that mixing of an isotropic compartment ($f_0=0.2$, $D_{\text{iso}}=3\times10^{-3}\text{mm}^2/\text{s}$) and two crossing fascicles represented by two single tensors ($f_1=f_2=0.4$, FA $=0.9$, diffusivity $=2.1\times10^{-3}\text{mm}^2/\text{s}$, crossing angle $=90^\circ$) using Equation 2 leads to a non-monoexponential decay *in the voxel*, even for b-values below $3000\text{s}/\text{mm}^2$. This illustrates that a non-monoexponential decay in a voxel may arise from a sum of mono-exponential behaviors.
doi:10.1371/journal.pone.0048232.g002

To the best of our knowledge, all approaches accounting for the non-monoexponential signal decay have considered the case of a single fascicle in each voxel. For example, Cheung *et al.* [60] have measured significant deviation from the Gaussian distribution with estimation of a single tensor and a single Kurtosis term with b-values as low as $b=2500s/mm^2$. However, as illustrated by Fig. 2, the intra-voxel orientation heterogeneity and the partial volume effect may be the predominant sources of the observed non-monoexponential decay at such diffusion scale. More precisely, while the presence of a non-monoexponential decay *for an individual fascicle* is commonly accepted when using very high b-values and short gradient pulse duration δ, its presence in data acquired with a clinical scanner with limited b-value range and large δ remains unclear. Particularly [15–17], suggest that the non-monoexponential behavior is negligible when considering b-values lower than $b\leq3000s/mm^2$, and that when the acquisition time or the available gradient strength is limited, a monoexponential *per-fascicle* model can be safely employed [16].

Therefore, in this work, we focused on a representation of each individual fascicle by a single tensor model. The *full multi-tensor model* estimation enables the assessment of individual fascicles characteristics in addition to the brain connectivity. Diffusion parameters (FA, MD, AD, RD) can be computed for *each* fascicle independently which is of central interest for fascicle integrity assessment. The number of parameters involved is relatively small, requiring a limited number of acquisitions for their estimation. However, full multi-tensor approaches have frequently been reported to be numerically challenging and unstable, experiencing difficulties for their estimation in practice. We show that this is due to inappropriate imaging acquisition settings leading to an under-determined system of equations, and we propose a complete solution.

Contributions

The contributions of this work are three-fold. First we provide the *theoretical* demonstration that multi-tensor models cannot be fully estimated with a single-shell HARDI acquisition because the tensor size and the fraction of occupancy are collinear, leading to a system of equations with an infinite number of solutions. With a single non-zero b-value, only the tensor orientation can be correctly estimated, but not the tensor size nor the fractions of occupancy. Multiple non-zero b-values are required to ensure a unique solution and to entirely estimate the full multi-tensor model, enabling simultaneous estimation of the tensor orientation, the tensor size and the fractions of occupancy.

Second, we propose a novel multi-tensor optimization technique based on the maximum *a posteriori* (MAP) principle. This allows us to combine the model estimation and the model regularization to reduce the effect of noise. Our prior is based on a finite difference scheme in which only tensors which are part of the same fascicle are regularized together. It is formulated in the log-Euclidean framework, which prevents leaving the set of symmetric positive definite matrices during the optimization and ensures non-degenerate solutions. Our formulation enables efficient optimization of the parameters and enables the introduction of suitable constraints on the estimated tensors.

Third, we propose to employ a novel acquisition scheme that enables estimation of a *full* multi-tensor model with optimal TE and consequently optimal SNR. Our CUbe and SPhere (CUSP) acquisition technique combines a single shell HARDI with images in the enclosing cube of constant echo time. We show that the enclosing cube of the shell is a *cube of constant TE*, in which gradients with varying b-values can be imaged without increasing the TE, by using gradients with norm greater than one. This satisfies the need for multiple non-zero b-values, enabling the estimation of the complete multi-tensor model. It incorporates high b-values which allows for better characterization of multi-compartment models [43,61]. We propose three ways to construct a CUSP acquisition based on a projected or a truncated multi-shell HARDI. The strength of our imaging technique is to achieve multiple b-values higher than the nominal b-value *while* achieving the same low TE as a single-shell HARDI. Compared to a multiple-shell HARDI, CUSP leads to a significantly higher signal-to-noise ratio, shorter imaging time and to potentially lower eddy current distortion.

The paper is organized as follows. We provide in Section 0.1 the theoretical demonstration that multi-tensor models require multiple non-zero b-values to be fully estimated. We describe our novel algorithm for estimating the parameters of the multi-fascicle model (MFM) in Section 2. We detail our Cube and Sphere (CUSP) imaging technique in Section 0.3. The CUSP-MFM evaluation includes several qualitative and quantitative experiments with both synthetic and in vivo data: angular resolution performance, comparison with the state-of-the-art ball-and-stick model and bootstrap experiments. We show that CUSP-MFM enables the characterization of multiple white-matter fascicles from short duration acquisitions compatible with routine clinical practice.

Materials

1 Theory: demonstration that multiple b-values are required

We demonstrate in this section that the tensors and fractions of occupancy of a multi-tensor model cannot be uniquely determined when using a single shell HARDI acquisition [62]. Consider a model with two fascicles represented by the two diffusion tensors $\widehat{\mathbf{D}}=(\widehat{\mathbf{D}}_1,\widehat{\mathbf{D}}_2)$ and the fractions $\widehat{\mathbf{f}}=(\widehat{f}_1,1-\widehat{f}_1)$, and let consider an acquisition with a unique non-zero b-value b. If $(\mathbf{D},\mathbf{f})$ are the underlying true tensors and fractions, then for any α, $\beta>0$ Equation 2 can be written as:

$$S_k\left(\widehat{\mathbf{D}},\widehat{\mathbf{f}}\right)=S_0\left(\frac{\alpha}{\alpha}\widehat{f}_1 e^{-b\mathbf{g}_k^T\widehat{\mathbf{D}}_1\mathbf{g}_k}+\frac{\beta}{\beta}(1-{}_1)e^{-b\mathbf{g}_k{}^T\widehat{\mathbf{D}}_2\mathbf{g}_k}\right)$$

$$=S_0\left(\alpha\widehat{f}_1 e^{-b\mathbf{g}_k^T\widehat{\mathbf{D}}_1\mathbf{g}_k-\log\alpha}+\beta(1-{}_1)e^{-b\mathbf{g}_k^T\widehat{\mathbf{D}}_2\mathbf{g}_k-\log\beta}\right)$$

Let y_k be the measured signal for the direction k and K the number of diffusion gradients. $\mathbf{D}$ and $\mathbf{f}$ are generally estimated by a least-square approach by considering:

$$\left(\hat{\mathbf{D}},\hat{\mathbf{f}}\right)=\arg\min_{\mathbf{D},\mathbf{f}}\sum_{k=1}^{K}\left[S_k(\mathbf{D},\mathbf{f})-y_k\right]^2 \tag{3}$$

Because $\mathbf{g}_k^T\mathbf{g}_k=1$, we have $\log\alpha=\mathbf{g}_k^T(\log\alpha\,\mathbf{I}_{3\times3})\mathbf{g}_k$ and:

$$\left(\hat{\mathbf{D}},\hat{\mathbf{f}}\right)=\arg\min_{\mathbf{D},\mathbf{f}}\sum_{k=1}^{K}\left[S_0\left(\alpha\widehat{f}_1 e^{-b\mathbf{g}_k^T\left(\widehat{\mathbf{D}}_1+\frac{\log\alpha}{b}\mathbf{I}_{3\times3}\right)\mathbf{g}_k}\right.\right.$$

$$\left.\left.+\beta(1-\widehat{f}_1)e^{-b\mathbf{g}_k^T(\widehat{\mathbf{D}}_2+\frac{\log\beta}{b}\mathbf{I}_{3\times3})\mathbf{g}_k}\right)-y_k\right]^2$$

We can show that for $\beta=\dfrac{1-\alpha\widehat{f}_1}{1-\widehat{f}_1}$ and $\alpha\in]0,1]$ then $\beta>0$ is satisfied and so are the fundamental properties of a mixture model: (1) the fractions sum to one, *i.e.* $\alpha\widehat{f}_1+\beta(1-\widehat{f}_1)=1$ and (2) each fraction is positive and not greater than one, *i.e.* $0<\alpha_1<1$ and $0<\beta(1-\widehat{f}_1)\leq 1$.

Consequently, when using a single non-zero b-value acquisition, then if $({}_1,1-{}_1)$ and $(\widehat{\mathbf{D}}_1,\widehat{\mathbf{D}}_2)$ is a solution of Equation 3, then for *any* $0<\alpha<1$, $\widehat{\mathbf{f}}'=(\alpha\widehat{f}_1,1-\alpha_1)$ and $\widehat{\mathbf{D}}'=(\widehat{\mathbf{D}}_1+\frac{\log\alpha}{b}\mathbf{I}_{3\times3},\widehat{\mathbf{D}}_2+\frac{\log(\frac{1-\alpha\widehat{f}_1}{1-{}_1})}{b}\mathbf{I}_{3\times3})$ is a solution of Equation 3 as well, because $S_k(\widehat{\mathbf{D}}',\widehat{\mathbf{f}}')=S_k(\widehat{\mathbf{D}},\widehat{\mathbf{f}})$ for all k. There is an infinite number of solutions. Additionally, non-degenerate tensors are obtained for $\alpha>e^{-b\lambda_1^{\min}}$, $\lambda_1^{\min}$ being the minimum eigenvalue of $\widehat{\mathbf{D}}_1$. The tensor size indicated by the magnitude of its eigenvalues and the partial volume fractions are collinear and cannot be uniquely determined. Intuitively it indicates that when using a single non-zero b-value, a decrease of the signal modeled by one of the tensors can be compensated for by an increase of the signal modeled by the other tensor, by transforming the tensor diagonals and the fractions.

It is not the case with multiple non-zero b-values b_k because $\widehat{\mathbf{D}}_1+\dfrac{\log\alpha}{b_k}\mathbf{I}_{3\times3}$ and $\widehat{\mathbf{D}}_2+\dfrac{\log\beta}{b_k}\mathbf{I}_{3\times3}$ are function of b_k. For example, if we consider two b-values b_1 and b_2, and separate the terms depending on b_1 corresponding to the indices $k=1,\ldots,K_{b_1}$ and the terms depending on b_2 corresponding to the indices $k=K_{b_1},\ldots,K$, it follows that:

$$\left(\hat{\mathbf{D}},\hat{\mathbf{f}}\right)=\arg\min_{\mathbf{D},\mathbf{f}}\sum_{k=1}^{K_{b_1}}S_0\left(\alpha\widehat{f}_1 e^{-b_1\mathbf{g}_k^T\left(\widehat{\mathbf{D}}_1+\frac{\log\alpha}{b_1}\mathbf{I}_{3\times3}\right)\mathbf{g}_k}\right.$$

$$\left.+\beta_2 e^{-b_1\mathbf{g}_k^T(\widehat{\mathbf{D}}_2+\frac{\log\beta}{b_1}\mathbf{I}_{3\times3})\mathbf{g}_k}-y_k\right)^2$$

$$+S_0\sum_{k=K_{b_1}+1}^{K}S_0\left(\alpha\widehat{f}_1 e^{-b_2\mathbf{g}_k^T\left(\widehat{\mathbf{D}}_1+\frac{\log\alpha}{b_2}\mathbf{I}_{3\times3}\right)\mathbf{g}_k}\right.$$

$$\left.+\beta\widehat{f}_2 e^{-b_2\mathbf{g}_k^T(\widehat{\mathbf{D}}_2+\frac{\log\beta}{b_2}\mathbf{I}_{3\times3})\mathbf{g}_k}-y_k\right)^2$$

A unique new multi-tensor model $(\widehat{\mathbf{D}}_1+\frac{\log\alpha}{b_k}\mathbf{I}_{3\times3},\widehat{\mathbf{D}}_2+\frac{\log\beta}{b_k}\mathbf{I}_{3\times3})$ does not satisfy $S_k(\widehat{\mathbf{D}},\widehat{\mathbf{f}})=S_k(\widehat{\mathbf{D}}',\widehat{\mathbf{f}}')$ for all k because, in contrast to the single non-zero b-value case, it depends on k. The use of multiple non-zero b-values enables a unique solution to be found and disambiguates the estimation of $\mathbf{f}$ and $\mathbf{D}$. This allows measurements of the fractions of occupancy and of each tensor size and orientation.

2 A novel multi-tensor parameter estimation procedure

We consider the image domain V to be a regular 3-dimensional (3D) grid, and consider the *full* multi-tensor model described by :

$$S_k(\mathbf{D},\mathbf{f}) = S_0(f_0 e^{-b_k D_{\text{iso}}} + \sum_{j=1}^{N_f} f_j e^{-b_k \mathbf{g}_k^T \mathbf{D}_j \mathbf{g}_k}),$$

Our aim is to recover the multi-tensor models $\mathbf{D}=(\mathbf{D}^i, i\in V)$ and the fractions $\mathbf{f}=(\mathbf{f}^i, i\in V)$ for each voxel of V. When estimating tensors, particular care must be taken to ensure the positive-definitive property of the $\mathbf{D}_j$ and to avoid degenerate tensors with null or negative eigenvalues. Although such tensors are non-physical, they commonly arise in high anisotropy regions or due to noise corruption [63]. Here we ensure the symmetric positive definite property of each tensor by parameterizing them in the log-Euclidean framework [64,65], by setting $\mathbf{L}^i=(\mathbf{L}_1^i,\ldots,\mathbf{L}_{N_f}^i)=(\log(\mathbf{D}_1^i),\ldots,\log(\mathbf{D}_{N_f}^i))$. It ensures that tensors with null or negative eigen-values are at an infinite distance. In contrast to Euclidean approaches, it does not require any particular care to preserve tensor attributes during the computation because all operations are performed within the appropriate manifold.

We denote by $\mathbf{y}$ the set of gradient images, with $\mathbf{y}_k^i$ denoting the i^{th} voxel of the gradient image k. The simultaneous estimation and regularization of $\mathbf{f}$ and $\mathbf{L}$ (and consequently $\mathbf{D}$) is performed according to a maximum *a posteriori* principle, by maximizing:

$$\begin{aligned}\widehat{\mathbf{L}}_{\text{MAP}},\widehat{\mathbf{f}}_{\text{MAP}} &= \arg\max_{\mathbf{L},\mathbf{f}} p(\mathbf{L},\mathbf{f}|\mathbf{y})\\ &= \arg\max_{\mathbf{L},\mathbf{f}} p(\mathbf{y}|\mathbf{L},\mathbf{f})p(\mathbf{f}|\mathbf{L})p(\mathbf{L}) \qquad (4)\\ &= \arg\max_{\mathbf{L},\mathbf{f}}[\ln p(\mathbf{y}|\mathbf{L},\mathbf{f}) + \ln p(\mathbf{f}|\mathbf{L}) + p(\mathbf{L})],\end{aligned}$$

which decomposes into a likelihood term and two prior terms. We assume statistical independence of the noise between the images and between the voxels, so that $p(\mathbf{y}|\mathbf{L},\mathbf{f}) = \Pi_{i\in V}\Pi_{k=1}^K\, p(\mathbf{y}_k^i|\mathbf{L}^i,\mathbf{f}^i)$. Furthermore, we assume a Gaussian noise with zero-mean and variance σ_k, and consider the following likelihood:

$$p(\mathbf{y}_k|\mathbf{L},\mathbf{f}) = \prod_{i\in V} \frac{1}{\sigma_k\sqrt{2\pi}} \exp\left(-\frac{\sum_{k=1}^{K} \|S_k\left(e^{\mathbf{L}^i},\mathbf{f}^i\right) - \mathbf{y}_k^i\|^2}{2\sigma_k^2}\right). \qquad (5)$$

The term $p(\mathbf{L})$ in Eq.4 enables us to incorporate a prior knowledge on the multi-tensor field $\mathbf{L}$. In this work we consider an anisotropic regularization prior that exploits spatial homogeneity but preserves sharp contours. More precisely, we favor smoothness of each $\mathbf{L}_j$ by setting $p(\mathbf{L}) = \Pi_{i\in V}\Pi_{j=1}^{N_f}\exp(-\alpha\phi(\|\nabla\mathbf{L}_j^i\|)$ where $\|\nabla\mathbf{L}_j^i\|$ is the norm of the spatial gradient of $\mathbf{L}_j^i$, and α is a parameter controlling the regularization strength. As generally employed, we set $\phi(s)=\sqrt{1+s^2/K^2}$ to account for *anisotropic* regularization, K being a normalization factor for the gradient. Following the one-tensor log-Euclidean model of [64] we set $\|\nabla\mathbf{L}_j^i\|^2 = \sum_{m=1}^3 \|\partial_{j,m}\mathbf{L}_j^i\|_{\text{LE}}^2$ with $\|\cdot\|_{\text{LE}}$ the log-Euclidean metric [65]. The regularization of multiple tensor models is, however, *not* the straight extension of the single-tensor case. Rather, only tensors which are part of the same fascicle should be regularized together. To achieve this, we propose an original approximation of the spatial gradient for the multiple tensor case. The partial derivative in a direction $\mathbf{i}_m$ ($m\in\{1,2,3\}$) is approximated by considering the two most similar neighbors $\mathbf{L}_q^{i\pm\mathbf{i}_m}$ to $\mathbf{L}_j^i$ in the following finite difference scheme:

$$\partial_{j,m}\mathbf{L}^i \approx \frac{\arg\min\limits_{\mathbf{L}_q}\|\mathbf{L}_q^{i+\mathbf{i}_m} - \mathbf{L}_j^i\|_{\text{LE}} - 2\mathbf{L}_j^i + \arg\min_{\mathbf{L}_q}\|\mathbf{L}_q^{i-\mathbf{i}_m} - \mathbf{L}_j^i\|_{\text{LE}}}{2\|\mathbf{i}_m\|} \qquad (6)$$

Note that this formulation is compatible when regularizing neighboring voxels containing a different number of tensors. A *softmax* approximation of the $\arg\min$ operator can be considered to ensure the differentiability of the regularization term. Indeed, by considering a finite set of measures $\{h(\mathbf{L}_q)\}_q$, $\arg\min_{\mathbf{L}_q} h(\mathbf{L}_q)$ can be approximated by:

$$\arg\min_{\mathbf{L}_q} h(\mathbf{L}_q) \approx \sum_{\mathbf{L}_q}\omega(\mathbf{L}_q)\mathbf{L}_q \quad \text{with} \quad \omega(\mathbf{L}_q) = 1 - \frac{e^{\gamma h(\mathbf{L}_q)}}{\sum_{\mathbf{L}_{q'}} e^{\gamma h(\mathbf{L}_{q'})}}.$$

This expression ensures $\omega(\mathbf{L}_q)\approx 1$ for the smallest $h(\mathbf{L}_q)$ and $\omega\approx 0$ for the others. Choosing a large value for γ allows faster transitions of ω between 0 and 1.

In this work we did not considered any prior knowledge on the estimated fractions and considered $p(\mathbf{f}|\mathbf{L})$ (see Eq.4) to be a uniform density. Ultimately, by considering constant noise characteristics across acquisitions, maximization of the posterior distribution in Eq.4 leads to the following minimization:

$$\begin{aligned}\widehat{\mathbf{L}}_{\text{MAP}},\widehat{\mathbf{f}}_{\text{MAP}} = \arg\min_{\mathbf{L},\mathbf{f}} \sum_{i\in V}\sum_{k=1}^{N_g}\left(S_k\left(e^{\mathbf{L}(\mathbf{x})},\mathbf{f}(\mathbf{x})\right) - \mathbf{y}_k(\mathbf{x})\right)^2 \\ + \alpha\sum_{j=1}^{N_f}\vartheta(\|\nabla\mathbf{L}_j(\mathbf{x})\|)\end{aligned} \qquad (7)$$

Euler-based parameterization of the tensor orientations. We parameterize each tensor's orientations with the Euler angle. We experimentally found this representation to enable a more efficient optimization of the parameters. In addition, it enables the choice of introducing various constraints to further reduce the number of parameters: symmetry of the eigenvalues (*e.g.* $\lambda_{11}=\lambda_{21}$), cylindrical shape of each tensor (*e.g.* $\lambda_{j2}=\lambda_{j3}$), bounds on the magnitude of the eigenvalues, equiplanar configuration for the tensors, and others.

Initialization. The model parameters are estimated by performing an iterative minimization which requires a starting point. As in [50] we initialize the multi-tensor fitting procedure by considering the one-tensor solution obtained by a robust least-squares estimate. We denote by $\mathbf{D}_{1\text{T}} = \mathbf{R}_{1\text{T}}^T\Lambda_{1\text{T}}\mathbf{R}_{1\text{T}}$ the one-tensor solution with eigen values $\Lambda_{1\text{T}} = \text{diag}(\lambda_1^{1\text{T}},\lambda_2^{1\text{T}},\lambda_3^{1\text{T}})$. To enable a faster convergence, the first two tensors $\exp\mathbf{L}_1^{(0)}$ and $\exp\mathbf{L}_2^{(0)}$ are initialized according to the rotation of $\mathbf{D}_{1\text{T}}$ of angle $\vartheta = \pm\frac{\lambda_2^{1\text{T}}}{\lambda_1^{1\text{T}}}\frac{\pi}{4}$. The rotation is applied in the plane formed by the two largest eigen values ($\lambda_1^{1\mathrm{T}}$,$\lambda_2^{1\mathrm{T}}$) and composed with a shrink of $\lambda_2^{1\mathrm{T}}$. In consequence, when $\lambda_1^{1\mathrm{T}} >> \lambda_2^{1\mathrm{T}}$, which is likely to indicate an individual fascicle in that voxel, the initial $\mathbf{D}_j$'s are two tensors with almost parallel principal diffusivities. In contrast, when $\lambda_1^{1\mathrm{T}} = \lambda_2^{1\mathrm{T}}$, the initial $\mathbf{D}_j$'s describe two tensors whose principal diffusivities are perpendicular. When estimating more than two tensors, the orientation of $\exp \mathbf{L}_{t\geq 3}^{(0)}$ is initialized with a random rotation of $\mathbf{D}_{1\mathrm{T}}$.

Numerical optimization. The solution of Equation 7 is obtained using the BOBYQA algorithm [66], a recent derivative-free bound-constrained optimization technique. BOBYQA is an iterative algorithm. At each iteration, it computes from a set of points a quadratic approximation for the objective function. The point giving the largest value for the objective function is replaced by the minimum of the quadratic approximation computed in a trust region. At each iteration the trust region is updated. BOBYQA converges faster than the Newton method and enables the introduction of constraints. The introduction of constraints on the f_j's enables the estimation of properly bounded fractions of occupancy ($f_j \in [0,1]$), while constraints on the Euler angles ensures the uniqueness of the Euler parameterization. We found it to be less sensitive to local minima than a conjugate gradient descent scheme. The numerical optimization is achieved by considering a diffusion model with gradually increasing complexity, starting from a simple stick model and finishing by the estimation of the *full* multi-fascicle model including the fractions of occupancy, the tensor orientations, the tensor eigen-values and the unrestricted water compartment. This makes the minimization less sensitive to the initialization, providing a robust full MFM estimate at each voxel.

3 The CUSP gradient encoding scheme

We have demonstrated in Section 0.1 that multiple non-zero b-values are required to fully estimate multi-tensor models. In this section we provide an optimal gradient encoding scheme which satisfies this requirement.

In diffusion weighted imaging, a key parameter in controlling the signal-to-noise ratio (SNR) is the echo time (TE). An increase in TE leads to a signal dropout due to T2 relaxation and therefore to a decrease in SNR (see [22], Eq. 1 and Fig. 1). Keeping the TE as low as possible is essential to acquire high quality measurements. However, the TE cannot be set to an arbitrary value, but is constrained by the choice of the nominal b-value $b_{\mathrm{nominal}} = \gamma^2\delta^2(\Delta - \delta/3)$ of the acquisition. The minimum achievable TE follows a complex relationship with b_{nominal} [9,10] which can be approximated [12] by:

$$\mathrm{TE} \approx \left(\frac{12 b_{\mathrm{nominal}}}{\gamma^2}\right)^{1/3}. \tag{8}$$

An ideal acquisition scheme for the estimation of a full multi-tensor model should (1) achieve multiple non-zero b-values and (2) achieve the optimal trade-off between imaging high b-values and minimizing the TE to maximize the SNR.

Single-shell HARDI as used in [19,45,48–50] to estimate a multi-tensor model employs gradients of constant strength $\|g_k\| = 1$ for each direction and provides a single-radius spherical sampling in q-space. Because the applied b-value is $b_k = b_{\mathrm{nominal}}\|g_k\|^2$, a single-shell HARDI acquires only a single non-zero b-value equal to b_{nominal}, which is not suited for the full estimation of multiple tensors. Separate single-shell HARDI scans with different nominal b-values can be employed to image multiple non-zero b-values. However, modifying the nominal b-value leads to a different TE for each scan (see Eq. 8). This causes different signal dropout artifacts between the scans and potentially different eddy current distortion, making the alignment of the DW images challenging and perturbing the MFM estimation. Additionally, acquisition of several separate single-shell HARDI is more prone to patient motion between the scans. Multi-shell HARDI combines in a single acquisition the sampling of multiple spheres in q-space by modulation of b_{nominal} with various gradient strengths $\|g_k\| \leq 1$. Because the unit-norm gradients $\|g_k\| = 1$ correspond to the shell of largest radius, this requires to set the nominal b-value based on the highest b-value of the acquisition. Since imaging of high b-values ($2000 s/mm^2$ or more) is known to provide a better separation of multiple fascicles and to facilitate the estimation of their orientation [14], a multi-shell HARDI with a high nominal b-value should be preferred. This, however, results in a substantially increased TE (see Eq. 8). This results in an increased acquisition time and a lower signal-to-noise ratio for *all* the measurements (see Eq. 1), impacting both the low and the high b-value measurements. Additionally, imaging a higher nominal b-value is generally achieved by using longer diffusion gradient pulses, which in turn leads to larger eddy current distortion.

We propose instead the novel CUbe and SPhere (CUSP) acquisition technique. We incorporate multiple non-zero b-values by combining a single-shell HARDI acquisition at a specified b_{nominal} with gradients lying in the enclosing cube of the shell [67]. More precisely, the single-shell HARDI uniformly samples the diffusion signal on the hemisphere, which is described by unit-norm gradients $\|g_k\| = 1$. This shell employs the b-value providing the optimal SNR for the diffusion weighted acquisition. It can be determined by $b_{\mathrm{optimal}} = 1.11/\mathrm{ADC}$ [10,68], and is often suggested to be $b_{\mathrm{nominal}} = b_{\mathrm{optimal}} = 1000\mathrm{s/mm}^2$ for an adult brain and $b_{\mathrm{optimal}} = 800\mathrm{s/mm}^2$ for a pediatric brain [69]. The single-shell HARDI provides a full spherical sampling with the optimal SNR and the optimal TE for the b-value b_{nominal}. We then acquire additional b-values$b_{k'} = b_{\mathrm{nominal}}\|g_k\|^2$ *without* modifying the TE by modulation of b_{nominal} with gradients whose *strengths is greater than 1*: $\|g_k\| > 1$. The only constraint for g_k is to have unit norm components, corresponding to the normalized current intensity in each gradient coil. Denoting by $g_k = \left[g_k^X, g_k^Y, g_k^Z\right]^T$ the gradient components, this leads to $|g_k^X| \leq 1, |g_k^Y| \leq 1, |g_k^Z| \leq 1$ which describes the enclosing cube of the sphere of radius $\|g_k\| = 1$. We call this region the *cube of constant TE*. Any gradient in this region can be acquired without modifying the TE by choosing the appropriate gradient strength. Because the diffusion sensitivity is dependent on the square of the gradient norm, imaging in the *cube of constant TE* enables the acquisition of b-values up to $3b_{\mathrm{nominal}}$. This maximum b-value is obtained when using the four non-symmetric $\sqrt{3}$-norm tetrahedral gradients [9] lying on the corners of the cube of constant TE ($|g_k^X| = |g_k^Y| = |g_k^Z| = 1$).

We envisage three ways to construct a CUSP acquisition which are based on a generalization of a multi-shell HARDI (see Fig. 3). First, in CUSP-T (Truncated), we consider a conventional multi-shell HARDI composed of $K \geq 2$ shells and truncate those parts of the shells that project outside the cube of constant TE of the inner shell (Fig. 3a). In this acquisition scheme, multiple shells with uniformly distributed b-values across the cube of constant TE are employed. However, the signal strength varies as $S_k(\mathbf{D}) = S_0 e^{-\mathrm{TE}/\mathrm{T2}} e^{-b_k \mathbf{g}_k^T \mathbf{D} \mathbf{g}_k}$ and so the SNR exponentially decreases with increasing b-value b_k. Therefore, in CUSP-xT (eXponential Truncated), we propose to employ shells with exponential spacing (Fig. 3b). The obtained exponentially increasing shell density with increasing b-value enables us to

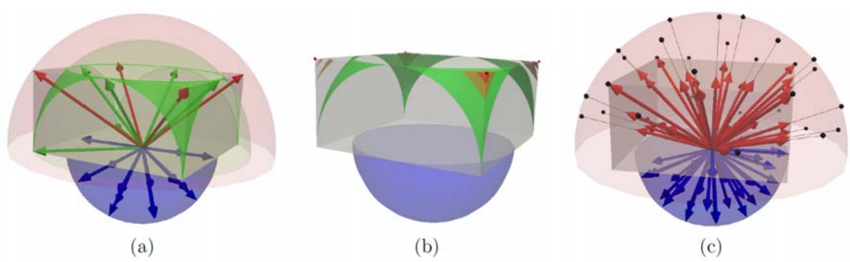

Figure 3. CUbe and SPhere (CUSP) imaging can be constructed as a truncated or a projected multi-shell HARDI. (a): In CUSP-T (Truncated), we consider a multi-shell HARDI with uniformly spaced radius (blue, green, red) and truncate those parts of the shells that project outside of the cube of constant TE of the inner shell. (b): CUSP-xT (eXponential Truncated) employs portion of multiple shells with exponentially spaced radius to achieve an improved uniformity of SNR. (c): In CUSP-P (Projected), we consider an inner shell at $b=b_{\text{nominal}}$ (blue) and an outer shell at $b=3b_{\text{nominal}}$ (red). The gradients of the outer shell are projected to the cube of constant TE (grey) to avoid any increase in TE. In these figures, the spherical and cubic sampling were shown in different partitions of q-space for visualization purpose.
doi:10.1371/journal.pone.0048232.g003

counter-balance the loss in SNR. This samples q-space in a manner that achieves an improved uniformity of SNR. Finally, in CUSP-P (Projected), we consider an acquisition composed of an inner shell at b_{nominal} and an outer shell at $3b_{\text{nominal}}$. The outer shell passes exactly through the corners of the cube of constant TE. Any other gradients of this shell are outside of the cube and cannot be imaged without modifying the TE. Instead, we propose to project them onto the faces of the cube of constant TE (Fig. 3c) by reducing the gradient strength until the cube surface is reached. This preserves the gradient orientations and provides high angular resolution imaging with a large number of different b-values above b_{nominal} without any additional cost in TE. The gradient scheme optimization algorithm of Cook *et al.* [70] can be used to identify maximally isotropic subsets of gradient orientations between the shells. Furthermore, if desired certain gradient directions and strengths can be fixed and others optimized around them.

Our work is the first report of utilizing such a CUbe and SPhere acquisition to enable the full estimation of a multiple fascicle model. The strength of our technique is to provide multiple non-zero b-values and higher b-values than the nominal b-value *while* achieving the same low TE as a single-shell HARDI. Consequently, it does not increase the imaging time, does not increase the eddy current distortion and provides the optimal signal-to-noise ratio for all the measurements.

4 Summary

We provided the theoretical demonstration that only the tensor orientation can be uniquely estimated when using a single non-zero b-value. Multiple non-zero b-values are required to fully estimate the tensors' direction in addition to the tensors' size and their respective fraction of occupancy. We proposed a novel algorithm for the estimation of the parameters of a multi-fascicle model (MFM). It is formulated as a log-Euclidean *Maximum A Posteriori* estimation problem. It ensures we estimate non-degenerate tensors and incorporates a finite difference spatial regularization scheme. In conjunction with our optimization algorithm we provided an optimal CUbe+SPhere (CUSP) imaging strategy based on a generalization of a multi-shell HARDI. It satisfies the requirement of multiple non-zero b-values and incorporates high b-values *while* employing the same minimum achievable TE as a single-shell acquisition. Consequently, the imaging time and the eddy current distortion are not increased. Compared to a multi-shell HARDI, CUSP achieves a better SNR. The performance and properties of our novel CUSP-MFM technique are investigated through several experiments described in the next section.

Methods

MFM estimation algorithm

The multi-tensor estimation algorithm was implemented in C++ and parallelized over the image space. The model parameters were set as follows. The diffusivity of free water at 37°C was set to $D_{\text{iso}}=3.0\text{x}10^{-3}\ \text{mm}^2/\text{s}$ [17]. The anisotropic regularization parameter K was set to 0.01 and the regularization influence parameter α progressively increased between $[0,\alpha_{\max}=1]$, playing the role of the inverse of a decreasing temperature as proposed in [71]. This allows to first explore a larger number of solutions (high temperature) and in a second step to constrain the solution by gradually increasing the weight of the neighborhood (low temperature). Since the minimization was performed with the BOBYQA algorithm, which is a derivative-free optimization technique, we used the original $\arg\min$ operator in Equation 6 and not its softmax approximation. Depending on our experiments, we considered a maximum of $N_f=2$ or $N_f=3$ tensors per voxel. The isotropic water fraction was initialized to $\mathbf{f}_0^{(0)}=0.1$ and the fascicle fractions to $\mathbf{f}_j^{(0)}=0.9/N_f$ for $j \in 1,\ldots,N_f$. All parameters may be estimated simultaneously with CUSP-MFM. However, in order to reduce the number of parameters, each tensor was constrained to have a cylindrical shape by setting $\lambda_{j,2}=\lambda_{j,3}$ for $j=1,\ldots,N_f$. A cylindrical shape was also employed in [15] and is generally considered reasonable with regard to the expected shape of a fascicle. Consequently, fitting our model involved the estimation of $5N_f$ free parameters: four parameters per tensor, and N_f parameters for the N_f+1 fractions. Model order selection was used to determine the number of fascicles at each voxel when appropriate. This was achieved by the F-test method [44]. A number of other model selection approaches have been investigated in the literature [43,44,61,72]. Their comparison, however, fall outside of the scope of this current work.

Two-tensor synthetic data

We generated various synthetic phantoms to evaluate CUSP-MFM. The tensor profile D_j representing an individual fascicle was chosen to match typical in vivo data observations. A trace of $\text{Tr}(D_j)=2.1\times10^{-3}\ \text{mm}^2/\text{s}$ was chosen [12], and varying FA for each tensor ($\text{FA}_1=0.9$; $\text{FA}_2=0.7$) simulated. This was achieved by considering the following relationship between the eigen-values $(\lambda_1,\lambda_2,\lambda_3)$ of a cylindrical tensor D_j and the tensor FA and trace $\text{Tr}(D_j)$: $(\lambda_1,\lambda_2,\lambda_3)=\text{Tr}(D_j)/3(1+2u,1-u,1-u)$ with $u=\text{FA}/\sqrt{3-2\text{FA}^2}$. The fractions for the isotropic compartment (f_0) and the tensors (f_1,f_2) were set to $(f_0,f_1,f_2)=(0.15,0.6,0.25)$.

The diffusion-weighted signal was simulated for different acquisition schemes and corrupted by various Rician-noise levels. The reported SNR were computed on the $b=0$ s/mm^2 images.

We focused here on short duration acquisitions with a low number of directions which are of practical interest for clinical applications. We considered a CUSP-T acquisition consisting of a total of thirty-five images, referred to as CUSP35 (Fig. 3a). CUSP35 was constructed from a *truncated three-shells HARDI* composed of five $b=0\mathrm{s/mm}^2$, an inner shell of sixteen directions at $b=1000\mathrm{s/mm}^2$, a second shell at $b_2=2000\mathrm{s/mm}^2$ and a third shell at $b_3=3000\mathrm{s/mm}^2$. The gradients of the inner shell were uniformly distributed on the hemisphere by minimizing the sum of the electrostatic repulsive forces [10]. The second shell was truncated to the cube of constant TE by imaging the six hexahedral gradients which are located at the intersection of the second shell and the edges of the cube of constant TE. The truncation of the third shell to the cube of constant TE led to the four $b=3000\mathrm{s/mm}^2$ tetrahedral gradients only. Two repetitions of these gradients were achieved [67] to counterbalance the lower SNR associated with such high b-value measurements.

We compared the CUSP35 acquisition scheme to a single-shell HARDI acquisition, referred to as HARDI35, which includes five $b=0\mathrm{s/mm}^2$ images and one shell of thirty directions at $b=1000\mathrm{s/mm}^2$. We also considered an acquisition scheme with five $b=0\mathrm{s/mm}^2$ and 251 unique directions (HARDI256). Again, we employed the electrostatic repulsion algorithm of [10] to determine uniformly distributed gradient orientations on the hemisphere for both HARDI35 and HARDI256. In the following, HARDI35-MFM and CUSP35-MFM refers to the MFM estimation performed by our novel algorithm with respectively the HARDI35 and the CUSP35 acquisition schemes. Identical estimation parameters were employed in HARDI35-MFM and CUSP35-MFM.

For each experiment we reported both qualitative and quantitative results. For the quantitative analysis, we compared the estimated multi-fascicle model to the synthetic ground truth by means of different metrics. The tensors were compared in term of average log-Euclidean distance (tALED), taking into account a possible permutation between the estimated and the reference tensors:

$$\mathrm{tALED}(D^{\mathrm{a}},D^{\mathrm{b}})=\min\big(||D_1^{\mathrm{a}}-D_1^{\mathrm{b}}||_{\mathrm{LE}}+||D_2^{\mathrm{a}}-D_2^{\mathrm{b}}||_{\mathrm{LE}}\ ,\ ||D_1^{\mathrm{a}}-D_2^{\mathrm{b}}||_{\mathrm{LE}}+||D_2^{\mathrm{a}}-D_1^{\mathrm{b}}||_{\mathrm{LE}}\big).$$

Using the log-Euclidean metric enables us to fully compare the tensors and not just the crossing angle as frequently done in the literature. The corresponding fractions were compared in terms of average absolute difference (fAAD). We also compared our multi-fascicle model to the ball and stick model [42] implemented in FSL. Since this model estimates only the fascicle orientations it was not possible to compare the full tensors nor to compare diffusion scalar parameters. We consequently compared our fitting algorithm to the ball-and-stick algorithm by assessing the average minimum angle (tAMA) [48] widely used in the literature. Finally, we simulated the diffusion signal arising from two uniform crossing fascicles, for various Rician noise corruption levels (50dB and 30dB). We carried out the MFM estimation and then characterized the uniformity of diffusion scalar parameters along the fascicles.

In vivo data

The performance of CUSP-MFM was assessed on in vivo data acquired on a Siemens 3T Trio scanner with a 32 channel head coil. The scanned subjects were all healthy volunteers, of age between 28 and 30 years old. The acquisition parameters used were as follows: 66 slices, FOV = 215mm, matrix = 120×120, resolution = 1.8×1.8×2.4mm^3. Eddy current distortion was minimized by utilizing a twice-refocused spin echo sequence [23]. In the first experiments, we employed the same gradient strength and orientation as those used in our synthetic experiments (CUSP35 and HARDI35). The minimum achievable TE/TR for both CUSP35 and HARDI35 were *identical* and equal to $\mathrm{TE}=86\mathrm{ms}/\mathrm{TR}=9500\mathrm{ms}$, achieving an acquisition duration lower than 6 minutes.

We acquired a multi-shell HARDI composed of 5 $b=0\mathrm{s/mm}^2$ and three shells of 20 gradient directions each at $b=1000\mathrm{s/mm}^2$, $b=2000\mathrm{s/mm}^2$ and $b=3000\mathrm{s/mm}^2$, referred to as MSHARDI-65. Maximally isotropic gradient subsets were obtained by using the algorithm of [70].

We acquired a CUSP-P acquisition referred to as CUSP65 and constructed from a *projected two-shell HARDI* (Fig. 3c) consisting of 5 $b=0\mathrm{s/mm}^2$ images, 30 gradients on the inner shell at $b=1000\mathrm{s/mm}^2$ and 30 gradients on the outer shell at $b=3000\mathrm{s/mm}^2$.

We employed a generalization of the optimization algorithm of [70] to determine maximally isotropic gradient subsets for such a CUSP-P. More precisely, we first optimized the subset of 30 gradients of the inner shell with the electrostatic repulsion model of [10], providing uniformly distributed gradient directions on the hemisphere. We then optimized the second subset of 30 gradients with the electrostatic repulsion model of [10] while (1) taking into account the repulsion in orientation with the first subset and (2) enforcing the inclusion of gradients at $b=2000\mathrm{s/mm}^2$ and $b=3000\mathrm{s/mm}^2$ to ensure that high b-value images are acquired and for comparison to the multi-shell HARDI. The gradients of this second shell were projected to the cube of constant TE to avoid any increase in TE (see Fig. 3c) compared to imaging the inner shell only. The TE for MSHARDI-65 and CUSP-65 was respectively 108ms and 78ms, and the acquisition time lower than 12 minutes.

Finally, a T1-weighted MPRAGE image was acquired with the following parameters: 160 slices, FOV = 205mm, matrix = 256×256, resolution = 0.8×0.8×1mm^3, TE = 2.27ms, TR = 1410ms, 3min 50sec. This anatomical scan was used to visualize the results.

The diffusion weighted images were corrected for head motion during the scan by rigid registration of the DW-images to the $b=0\mathrm{s/mm}^2$ image [73]. The gradient orientations were compensated for the rotation component of the transformation for each image. We considered the estimation of $N_f=2$ and $N_f=3$ fascicles, with and without employing the F-test model selection. The multi-fascicle model estimation time was approximately 1 hour and 30 minutes for $N_f=2$ and 2 hours for $N_f=3$ on a 8 Core 3 Ghz Intel Xeon. We compared the $N_f=2$ fascicles case with the ball-and-stick model implemented in FSL [42]. We also estimated the ball-and-stick model after noise correction of the DW images with the Joint Linear Minimum Mean Squared Error (LMMSE) filter proposed by [74].

We performed an experiment to examine the effect of CUSP-MFM on the assessment of tensor diffusion parameters. We applied 20 random rotations to both the in vivo CUSP35 and HARDI35 acquisitions. This simulates variations of the partial volume effect in each voxel, and consequently variations of the partial volume fractions of each tensor in each voxel. However, the fractional anisotropy should be stable across the rotations. We selected a fascicle of the corticospinal tract and assessed the fraction anisotropy along this same tract for the multiple rotations. We compared the results when using CUSP and the single-shell HARDI.

Finally, a *quantitative* comparison of CUSP to a multi-shell HARDI was achieved by assessing the estimation uncertainty via *residual bootstrapping* [75]. The residual bootstrap is a model-based resampling technique. It is based on the estimation of a model (here the multi-fascicle model) and on the generation of a set of virtual new DWI acquisitions by randomly sampling the model residuals. In contrast to repetition-based resampling techniques, it does not require any repetition of the gradient directions during the acquisition. Contrary to the wild bootstrap [76], it does not assume any symmetry in the distribution of the residuals. The residual bootstrap has been shown to lead to smaller biases and reduced overall errors in comparison to the wild bootstrap, enabling the estimation of uncertainties with higher accuracy [75]. Here, the residual bootstrap method was employed to quantitatively compare the estimation uncertainty with CUSP-65 and with MSHARDI-65.

Results

Synthetic data

We generated a set of phantoms containing one hundred two-tensor models separated by a given angle *with various orientations* (see Fig. 4a). Ten phantoms with crossing angles from 0 to 90° were generated. Fig. 4 qualitatively shows the improvement when estimating the tensors from the CUSP35 acquisition (Fig. 4b) compared to a single-shell HARDI35 acquisition (Fig. 4c). Both the tensors and the fraction f_1 are more uniform with CUSP35-MFM.

Fig. 5 quantitatively reports the estimation accuracy for various SNR (50dB, 30dB). It shows for each angle (from 0° to 90°) the mean and variance of the tALED and fAAD metrics over the one hundred tensors. Particularly, it shows the CUSP35 encoding scheme achieves better results than HARDI35 and HARDI256. It experimentally supports our theoretical demonstration that multiple non-zero b-values are required to fully estimate the tensors. Employing even up to 251 unique directions does not dramatically improve the results since it does not solve the collinearity of the parameters.

Fig. 6 shows the comparison of our MFM algorithm to the the ball-and-stick algorithm implemented in FSL [42]. We noticed that FSL does not perform well with the CUSP35 acquisition scheme. CUSP35-MFM provides the best angular resolution compared to the other approaches, particularly for small angles, while it provides more information by estimating the full tensors. With CUSP-MFM, each fascicle can be characterized by evaluating the diffusion tensor parameters (FA, MD, etc.) of each tensor.

Finally, we investigated whether or not CUSP introduces an angular preference for certain spatial directions when characterizing fascicles (Fig. 7). We simulated the DW-images for a single tensor with constant FA ($FA = 0.9$) with various orientations, for both the CUSP and the multi-shell HARDI acquisitions. The tensor was rotated around its third eigenvector by increments of 5 degrees between 0 and 360 degrees. For each orientation, the tensor representing the fascicle was estimated, and its FA assessed. This was repeated one hundred times. Fig. 7 shows the mean FA for each tensor orientation over the hundred repetitions. The mean FA obtained with a multi-shell HARDI and with CUSP are comparable, showing that such a multi-shell HARDI and CUSP have a uniform angular sensitivity to fascicle orientation.

We then generated a phantom representing two uniform fascicles ($FA_1 = 0.9$; $FA_2 = 0.7$) crossing with an angle of 60° (see Fig. 8). In this experiment, the F-test model selection was used. The resulting multi-tensor field is reported in Fig. 7a. It shows more uniform tensors when using CUSP35-MFM. Fig. 7b reports the estimated fraction f_0 of the isotropic diffusion compartment. It shows that CUSP35-MFM provides an estimate of f_0 very close to the true simulated value (0.15), while the isotropic water fraction cannot be accurately estimated with HARDI35-MFM. Finally, Fig. 7c depicts the FA (non-)uniformity along the fascicles. For illustration, we modified the z-coordinate of the tract streamlines to encode for the FA along the tract. It shows that CUSP35-MFM provides a much more uniform FA than HARDI35-MFM.

These findings were quantitatively verified by simulating one hundred times the diffusion signal for different signal-to-noise ratios (50dB and 30dB). Fig. 9 reports the mean and variance of the FA (Fig. 9a) and of the radial diffusivity (RD) (Fig. 9b) over these experiments. With CUSP35-MFM, the FA and the RD of

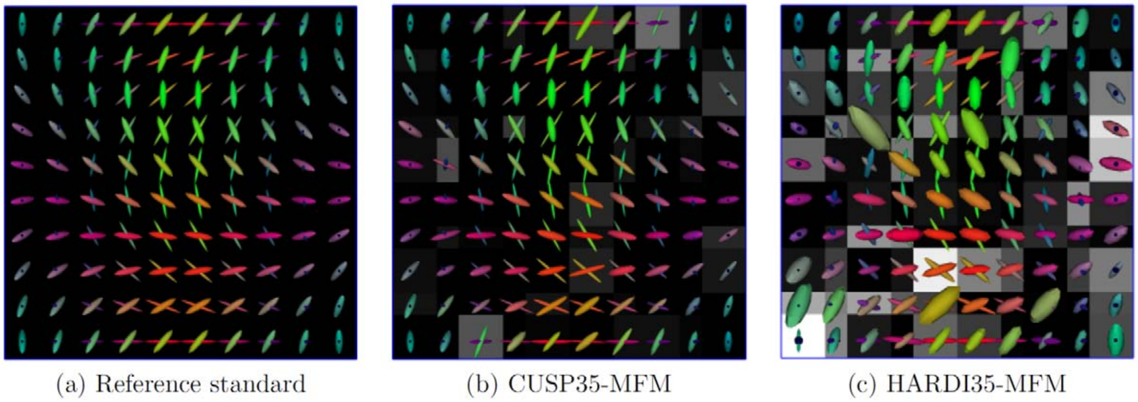
(a) Reference standard
(b) CUSP35-MFM
(c) HARDI35-MFM

Figure 4. Qualitative evaluation of CUSP-MFM. (a) One hundred synthetic tensors crossing at 50° in various configurations. (b) Estimated tensors with a CUSP35 gradient encoding scheme ($SNR = 30dB$) superimposed on the first tensor's fraction f_1 (window: 0.2 ; level 0.7). (c) Estimated tensors with the HARDI35 gradient encoding scheme. With a single non-zero b-value (Fig. c), the tensor eigenvalues and the fractions are collinear, leading to a poor multi-fascicle estimate. When using CUSP35 (Fig. b), the system is better determined, leading to a better estimate. Both the tensors and the fraction f_1 are more uniform when using CUSP35-MFM compared to HARDI35-MFM.
doi:10.1371/journal.pone.0048232.g004

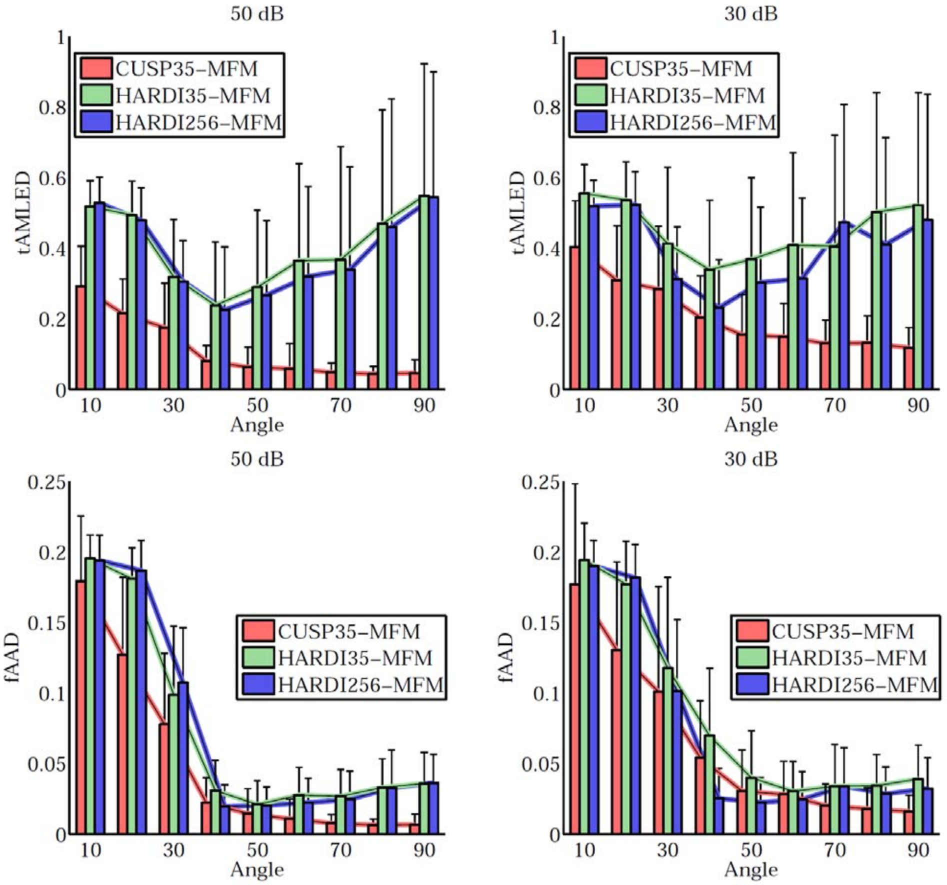

Figure 5. Quantitative evaluation of the CUSP-MFM estimation accuracy. Quantitative evaluation of the estimation accuracy for the fractions (first line, fAAD metric) and the tensors (second line, tALED metric). Each plot shows the quality metric (fAAD, tALED) in function of the crossing angle for various gradient encoding scheme and various signal-to-noise ratios. It shows that employing a large number of directions (HARDI256) does not dramatically improve the results whereas introducing multiple non-zero b-values does (CUSP35). CUSP35-MFM consistently provides the best estimation accuracy.
doi:10.1371/journal.pone.0048232.g005

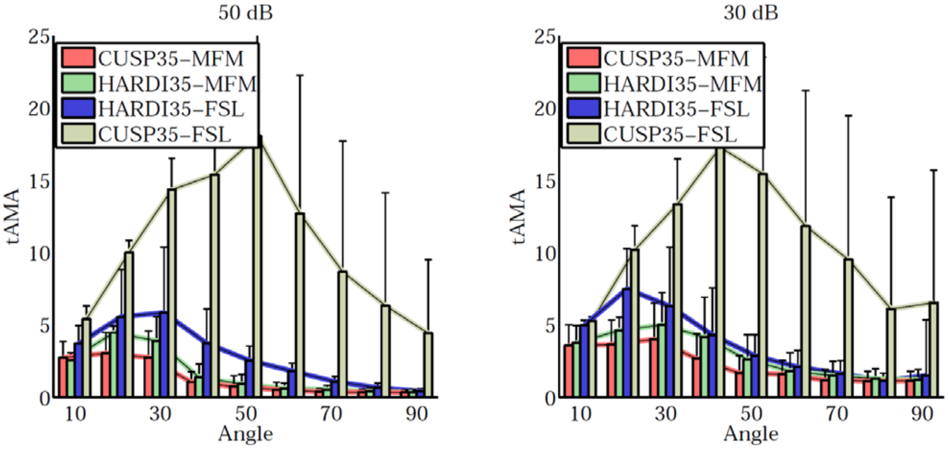

Figure 6. Quantitative evaluation of the angle detection accuracy. Evaluation of the angle detection accuracy in term of average minimum angle error (tAMA) and comparison with the ball-and-stick model of FSL. CUSP35-MFM provides on average the best angular resolution, particularly for angles lower than 50 degrees, while it provides more information for clinical studies by estimating the full tensors: diffusion parameters such as the fractional anisotropy or the radial diffusivity can be computed for each fascicle independently.
doi:10.1371/journal.pone.0048232.g006

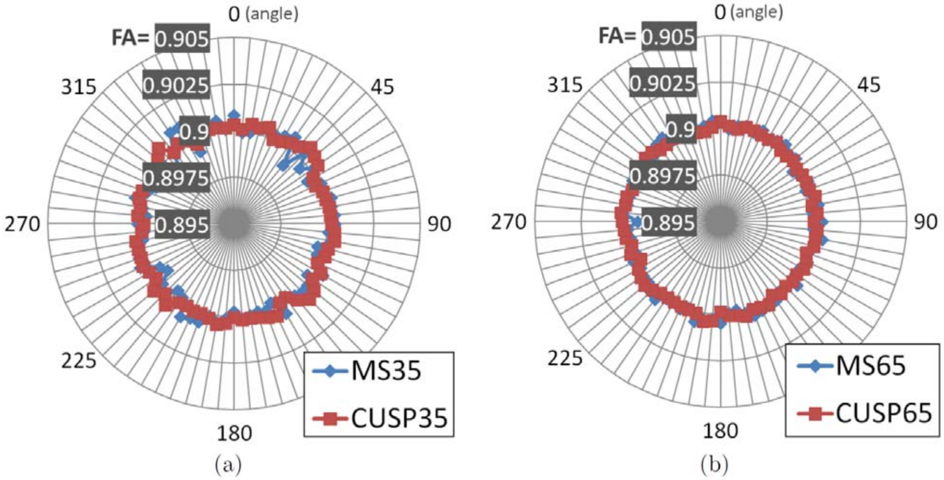

Figure 7. Angular dependency of the fractional anisotropy with CUSP and a multi-shell HARDI. The DW-images for a single tensor with constant FA (FA $=0.9$) were simulated one hundred times for various tensor orientations (0–360°) and for both CUSP and a multi-shell HARDI, corrupted by Rician noise (SNR on the $b=0\mathrm{s/mm^2}$: 25dB). We report the mean of the estimated FA for each angle, for CUSP-35 (a) and CUSP-65 (b). The average FA is compared to the average FA obtained when using MSSHELL-35 (MS35: 5 $b=0\mathrm{s/mm^2}$ and three shells of 10 gradients each at $b=1000\mathrm{s/mm^2}$, $b=2000\mathrm{s/mm^2}$, $b=3000\mathrm{s/mm^2}$) and MSSHELL-65 (MS65). The angular dependency of CUSP and of a multi-shell HARDI is similar.
doi:10.1371/journal.pone.0048232.g007

two uniform fascicles is distinctly more uniform than with HARDI35-MFM, which is highly relevant to accurately characterize the fascicles.

In vivo data

We report in this section the results of experiments on in vivo data. In Fig. 10, we qualitatively compare the multi-tensor estimation performances when using a HARDI35 acquisition scheme (first column) and a CUSP35 acquisition scheme (second

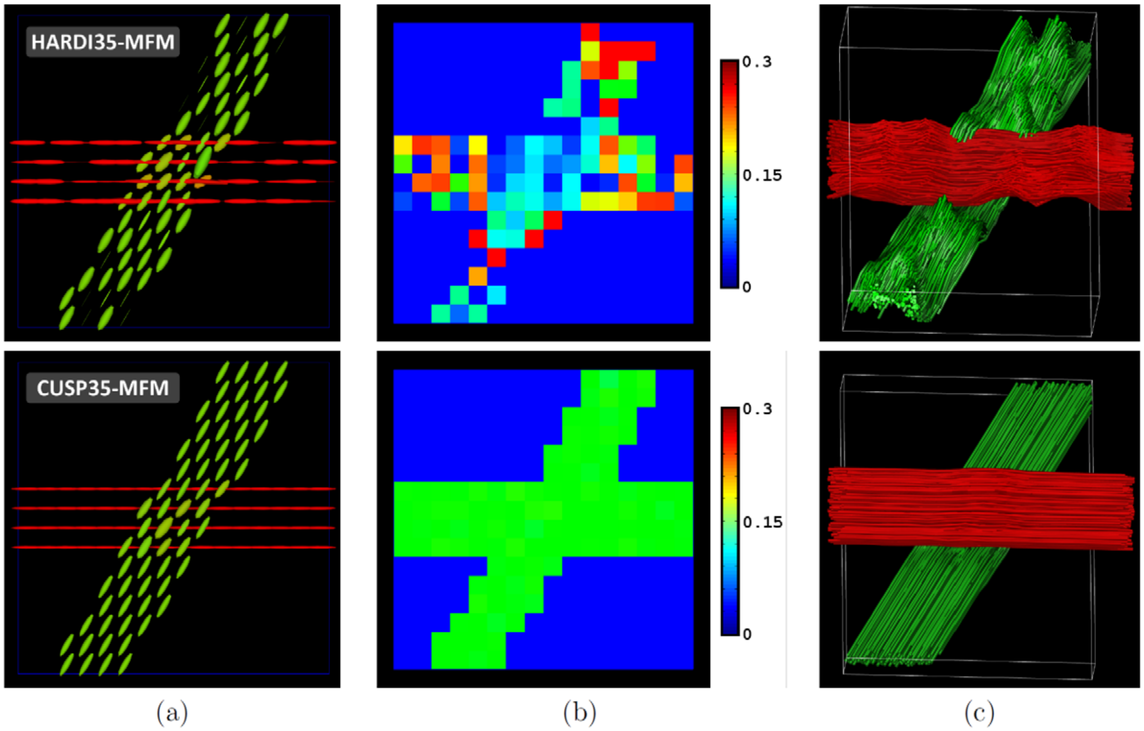

Figure 8. Two uniform crossing fascicles have uniform characteristics (FA) with CUSP-MFM. Estimation of two synthetic crossing fascicles (angle $=60^{\circ}$, SNR $=30$dB) with HARDI35-MFM (first line) and with CUSP35-MFM (second line). (a) Estimated tensors and (b) fraction of the isotropic water compartment. (c) Illustration of the fractional anisotropy uniformity for each fascicle. In this image, the z-coordinate of the tract streamlines encode for the fractional anisotropy along the tracts (red: FA $=0.9$; green: FA $=0.7$). It shows the FA of two uniform fascicles to be qualitatively more uniform with CUSP35-MFM than with HARDI35-MFM.
doi:10.1371/journal.pone.0048232.g008

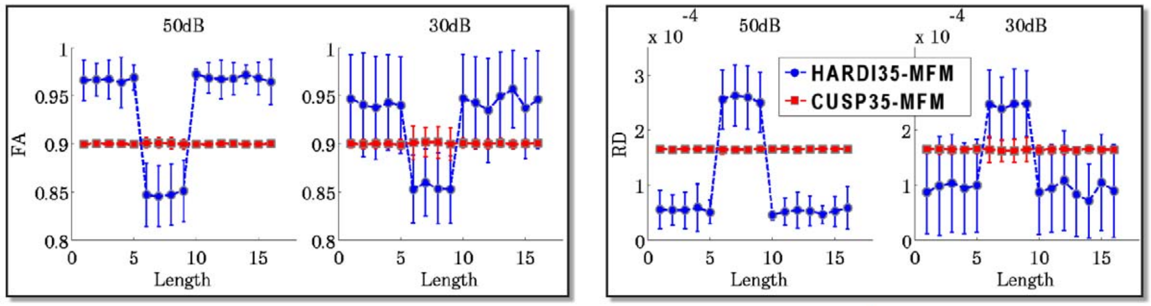

(a)

(b)

Figure 9. Quantitative evaluation of the fascicle characteristics along a uniform fascicle. Quantitative evaluation of diffusion parameters along the horizontal synthetic tract of Fig. 8 for SNR of 50dB and 30dB and for HARDI35-MFM and CUSP35-MFM. (a) Fractional anisotropy assessment. (b) Radial diffusivity assessment. It shows the FA and the RD of two uniform fascicles to be almost uniform with CUSP35-MFM, which is clinically relevant to assess individual fascicle characteristics when studying white matter development or degeneration.
doi:10.1371/journal.pone.0048232.g009

column). In this experiment, to fully characterize our multi-fascicle model approach, we did not employ any *model order selection* but estimated $N_f = 2$ tensors at each voxel. Tensors with estimated fraction of occupancy lower than 0.05 were, however, not visualized. In the first line we compare the results of HARDI35-MFM (Fig. 10a) and CUSP35-MFM (Fig. 10b). HARDI35-MFM leads to tensors with degenerate tensor size (areas 1), and leads to non-null tensors in the CSF (area 2), confounding isotropic water fraction and mixture of fascicles. In contrast, CUSP35-MFM achieves a better tensor uniformity.

Fig. 10c and Fig. 10d reports the results of HARDI35-MFM and CUSP35-MFM but *without* the estimation of the isotropic compartment. It shows that ignoring the isotropic compartment has substantially more impact when using CUSP35 (see Fig. 10d). Fig. 10e and Fig. 10f reports the results of the ball and stick model of FSL. It results in distinct estimated sticks in the body of the corpus callosum (area 3), a region known to contain a single fascicle orientation, probably fitting the noise. Additionally, sticks with orientations matching poorly the known anatomy are estimated (area 4). Thirty-five directions is perhaps not enough for this MCMC Bayesian ball-and-stick model to be accurately estimated. Applying a preprocessing noise-correction filter (Fig. 10g and Fig. 10h) improves the results but creates anatomically implausible crossings (areas 5 and 6).

Fig. 11 reports, for the same coronal slice, the MFM estimation results with $N_f = 3$ fascicles at each voxel *without* model order selection. Again, HARDI35-MFM leads to tensors with a degenerate size, and confounds the estimation of the isotropic water fraction and of the fascicles. In contrast, with CUSP35-MFM, the location of voxels in which three distinct fascicles are estimated with non-null fractions matches the known anatomy, whereas only 35 images were acquired. Additionally, the estimated orientation in the body of the corpus callosum matches the anatomy, whereas $N_f = 3$ tensors were estimated at each voxel.

In Fig. 12, we show the CUSP-MFM estimation results when using the CUSP-65 acquisition and the F-test model order selection with a maximum of $N_f = 3$ fascicles. Again, it shows estimated tensors that match the anatomy. Particularly, the outlined three tensor models correspond to a known region in the centrum semiovale where three fascicles are crossing.

Fig. 13 demonstrates how CUSP-MFM enables the estimation of the *full* multi-tensor, including the fractions of occupancy of each tensor. We performed various rotations of the diffusion-weighted images to simulate various partial volume effects. We considered a reference tract belonging to the corticospinal tract (see Fig. 13a), applied the same rotation to each tract point, and assessed the fractional anisotropy *along the tract* across the rotations. Fig. 13b shows the variance of the FA when the MFM is estimated without any regularization, with CUSP35 and with HARDI35. It shows that the FA variance is much larger with HARDI35, because using an acquisition with a single non-zero b-value does not enable the full multi-tensor estimation. In contrast, the FA variance is reduced with CUSP35. Fig. 13c shows that when adding the regularization, the FA variance is reduced for both HARDI35 and CUSP35. However, as shown on Fig. 13d, adding the regularization has a significant impact on the mean of the FA with HARDI35, but not with CUSP35. With HARDI35, the regularization better constrains the optimization but leads to a wrong solution. In contrast, CUSP-MFM enables estimation of the full multi-tensor model, and consequently estimation of diffusion tensor parameters which do not vary with the partial voluming nor the regularization.

Finally, we report in Fig. 14 the results of the residual bootstrap analysis, illustrating the benefits of employing CUSP instead of a multi-shell HARDI. From the initially fitted multi-fascicle model, we generated five hundred new virtual acquisitions. For each virtual acquisition, we estimated at each voxel the MFM and computed the maximum FA of the estimated fascicles. The maximum FA was used as a proxy to identify the same fascicle across multiple iterations of the bootstrap analysis. Fig. 14a and Fig. 14b shows the variance of the FA of the fascicle with the largest FA over the five hundred bootstrap iterations, respectively for MSHARDI-65-MFM and CUSP-65-MFM. It shows the uncertainty when estimating the fascicle of higher FA at each voxel. The uncertainty in FA is significantly lower with CUSP compared to the multi-shell HARDI, because MSHARDI-65 requires a larger TE to achieve a *nominal* b-value of $3000\mathrm{s/mm}^2$ which leads to an acquisition with lower SNR.

Discussion

Several methods have been investigated to overcome the limitations of DTI and to represent multiple white matter fascicles from diffusion-weighted imaging. Approaches such as DSI, QBI, EQBI, DOT, SD or GDTI focus on estimating the global shape of the diffusion profile resulting from multiple fascicles present in each voxel. The major drawback is they do not consider each fascicle independently. Consequently, they do not enable characterization of each fascicle, and do not enable comparison of the fascicle characteristics between individuals. The assessment of

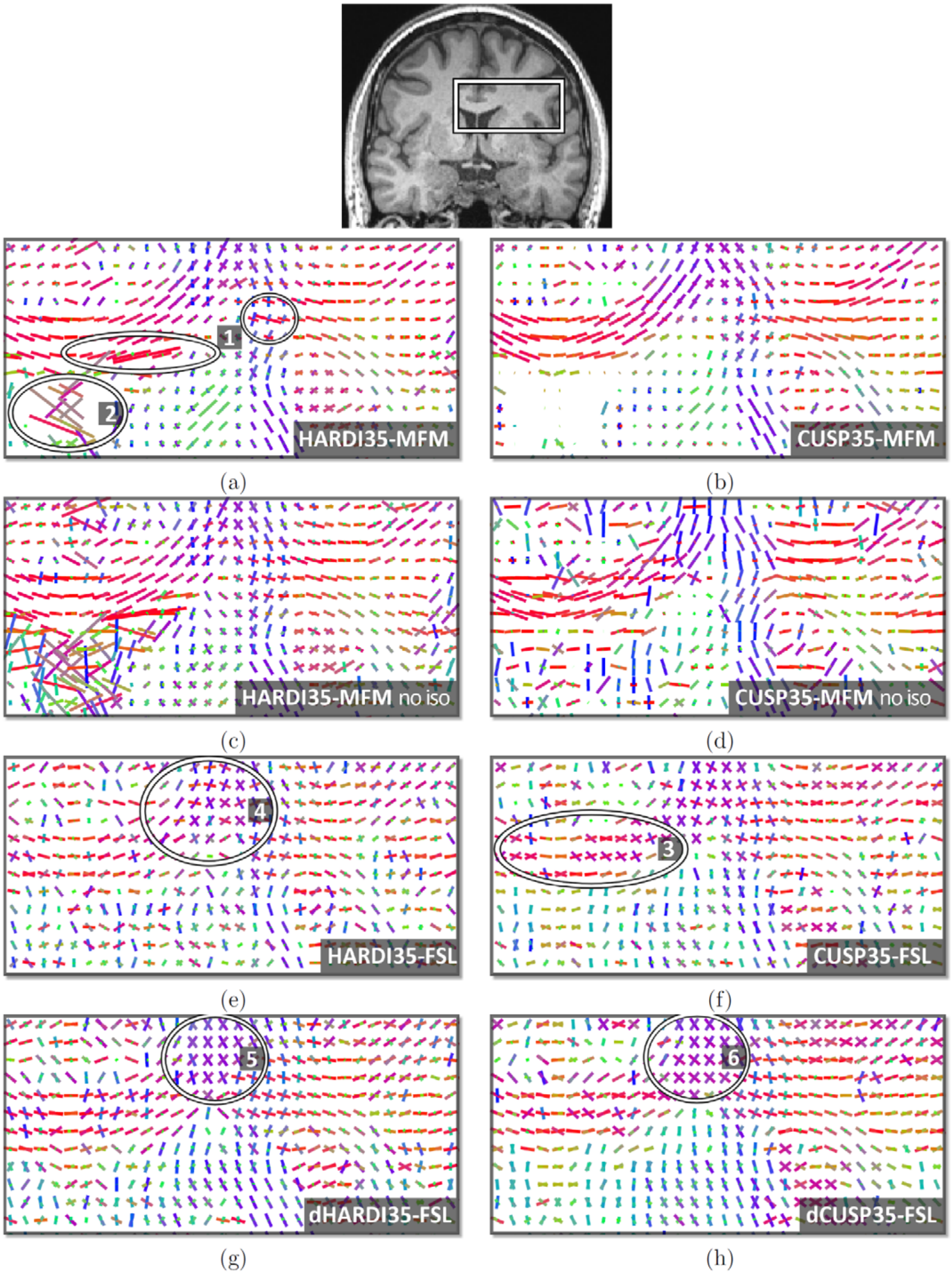

(a) (b)

(c) (d)

(e) (f)

(g) (h)

Figure 10. Evaluation with in vivo short duration DWI acquisitions with $N_f = 2$, without any model selection. Comparison of the HARDI35 (first column) and CUSP35 (second column) acquisitions. Fig.a and Fig.b: in contrast to CUSP35-MFM (b), HARDI35-MFM (a) leads to degenerate tensors (area 1) and confounds CSF contamination and fascicles (area 2). Fig.c and Fig.d: when ignoring the estimation of the isotropic compartment, the performance of CUSP35-MFM (d) are strongly affected. The diffusion of unrestricted water cannot be ignored when using a multiple b-values acquisitions. Fig.e and Fig.f: FSL estimates sticks with noisy orientation (area 4), and leads to non-aligned sticks in a single fascicle region of the corpus callosum (area 3). Fig.g and Fig.h: FSL estimation after denoising the DW images (dHARDI35 and dCUSP35).
doi:10.1371/journal.pone.0048232.g010

parameters such as the generalized fractional anisotropy (GFA) or the generalized mean diffusivity (GMD) has also been proposed [41]. However, these measures do not represent a fascicle property but a *dispersion property* of the diffusion signal inside each voxel. For example, a synthetic uniform fascicle can be simulated by considering an identical tensor at each voxel. Such a uniform fascicle crossed by another synthetic fascicle has a GFA that varies in the crossing region [41] because the dispersion of the diffusion signal is different in the crossing region. Therefore, the GFA which represents a voxel property provides misleading data. A uniform fascicle should have constant diffusion parameters along its path. This essential limitation reduces the scope of DSI, QBI, EQBI,

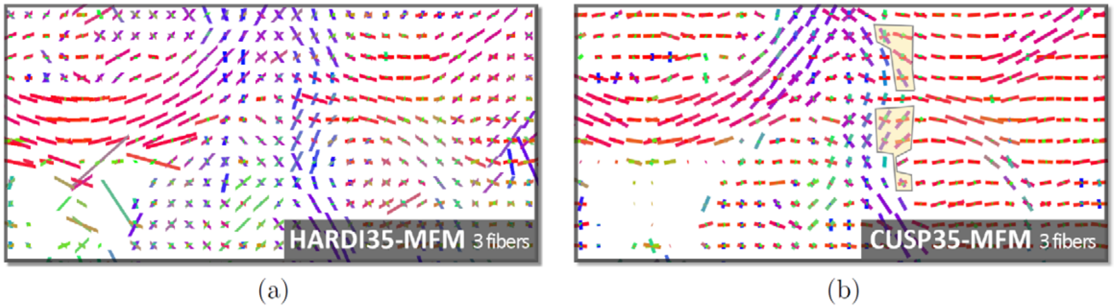

(a) (b)

Figure 11. Evaluation with in vivo short duration DWI acquisitions with $N_f = 3$ fascicles, without any model selection. Estimation of $N_f = 3$ fascicles with HARDI35 (a) and with CUSP35 (b), which contain only 35 images. The tensors with fraction of occupancy smaller than 0.05 were not visualized. CUSP35-MFM results in the estimation of three fascicles in a region (see outlined voxels) that matches the known anatomy, the centrum semiovale.

doi:10.1371/journal.pone.0048232.g011

DOT, or GDTI to connectivity analysis. In addition, these approaches generally require a relatively high number of DWI acquisitions, limiting their use in clinical practice. Recently, Raffelt *et al.* [77] have demonstrated through Monte Carlo simulations of a model of diffusion in cylinders of a certain size range with certain permeability characteristics, that the signal measured by a single shell HARDI acquired at $b = 3000\mathrm{s/mm}^2$ (with timing parameters achievable on a clinical MRI scanner) arises primarily from restricted water. Under these assumptions, the amount of signal can be related to the underlying density of white matter fascicles, thus enabling the formation of a measure of the 'apparent fiber density'. In addition, the orientation of white matter fascicles can be determined from the local signal maxima.

In contrast, our model enables the determination of the orientation of the white matter fascicles, measures of their local diffusion properties and the characterization of an unrestricted water component that is important in assessing edema and inflammation. Multi-fascicle approaches generally require the determination of the number of white matter fascicles at each voxel. This and only this enables characterization of each fascicle in addition to the orientation information, which is of central interest to study the white matter development or degeneration in research and clinical practice. Recently [78], have proposed to estimate a general ODF at each voxel and then fit tensors on the ODF to extract geometric features of the peaks. However, this requires the estimation of the ODF, which is sensitive to noise and requires a high number of DW images. In contrast, direct estimation of a MFM from the DW images enables representation of multiple fascicles and involves a small number of parameters, requiring potentially a small number of acquisitions. MFMs allow the computation of diffusion parameters such as the FA for each fascicle, which is essential for straightforward characterization of multiple fascicles.

Multi-tensor models have however frequently been reported to be numerically challenging and unstable [43,44,48]. Among others, Kreher *et al.* [44] have observed that with a model including one entirely isotropic diffusion tensor and multiple entirely anisotropic tensors, the mean diffusion and the relative ratio of components could not be separated with DW images measured at a single high b-value. In this paper we have shown that the reason lies in a collinearity in the parameters when a single non-zero *b*-value acquisition is employed, leading to an infinite number of solutions. With only one non-zero b-value, as often used in the literature [19,45,48–50], the *tensor size* indicated by the magnitude of its eigenvalues and the estimated *volume fractions* are *collinear*. Consequently, fitting them together may make a fascicle with a uniform $\mathbf{D}_1$ across its entire length grow and shrink as it passes through voxels and experiences different partial

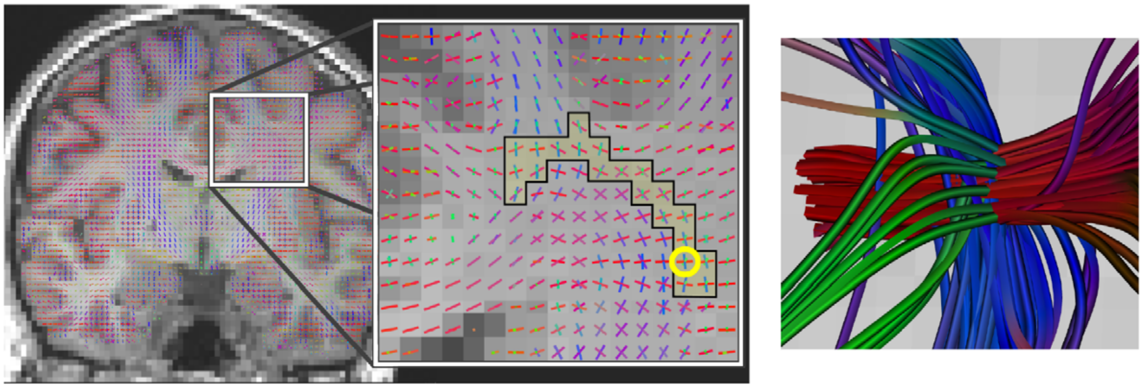

(a) (b)

Figure 12. Estimation of $N_f = 3$ fascicles with F-test model order selection and CUSP-65. (a) Estimated MFM superimposed on the T1-weighted anatomical image. Particularly, three tensor were correctly estimated in the centrum semiovale, which is a known brain region in which three fascicles are crossing. (b) Illustration of the tractography streamlines passing through the voxel encircled in yellow in (a), showing the three crossing fascicles.

doi:10.1371/journal.pone.0048232.g012

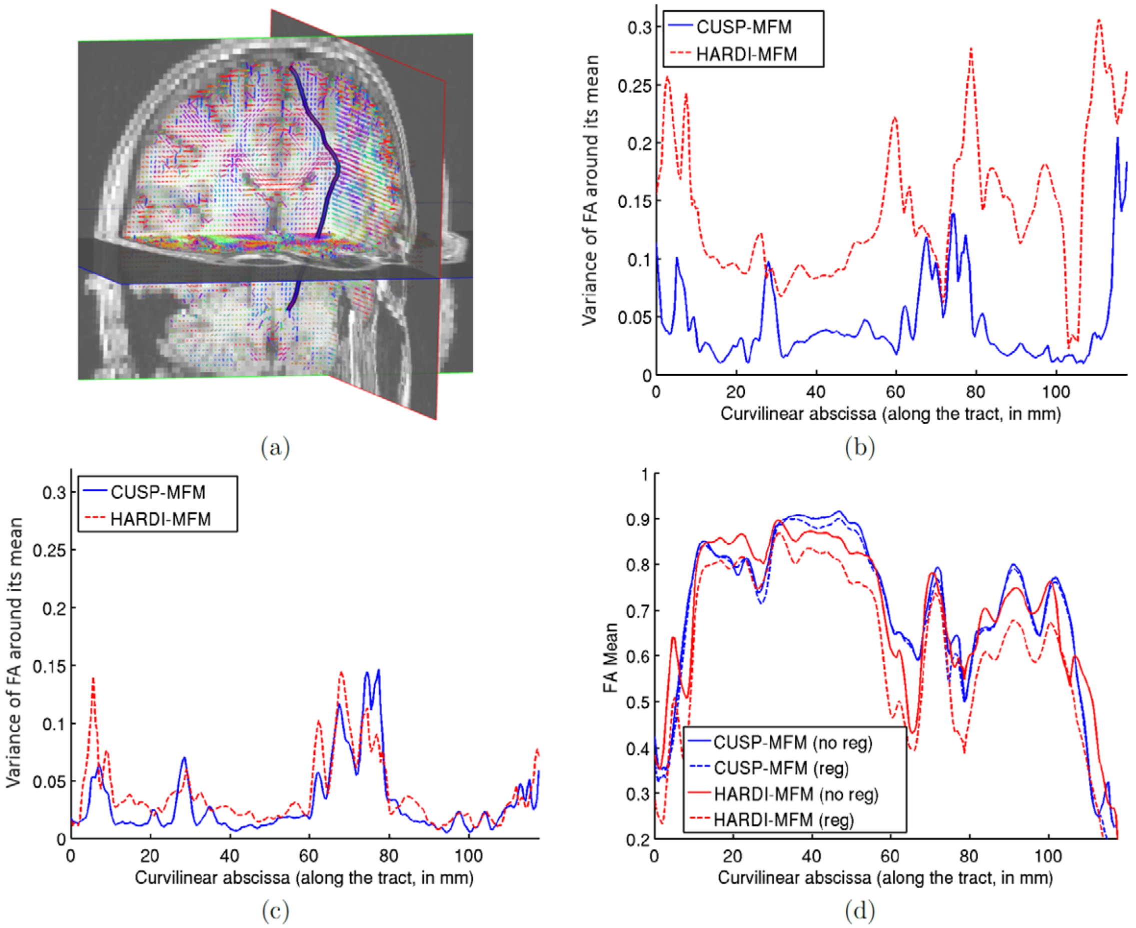

(a) (b)

(c) (d)

Figure 13. CUSP-MFM enables the estimation of diffusion tensor parameters which do not vary with the partial volume effect. We computed the FA along a same tract (Fig.a) for various artificial rotations of the diffusion-weighted images. For each streamline point, the most aligned anisotropic tensor with the streamline orientation was selected and its FA assessed. Fig.b shows the variance of the FA along the tract across the rotations, when using the CUSP or the HARDI acquisition and the MFM estimator without regularization and with the same parameters. HARDI has dramatically increased variance, as it conflates tensor size with partial voluming. CUSP does not. Fig.c shows the FA variance when adding the regularization to the estimation with both CUSP and HARDI. Fig.d shows the corresponding value of the FA along the tract. It shows that CUSP-MFM enables estimation of diffusion tensor parameters which do not vary with the partial volume fractions nor the regularization.
doi:10.1371/journal.pone.0048232.g013

volume effects. Algebraically one constraint in the modeling could resolve this ambiguity: imposing a symmetry between the tensors' eigenvalues such as $\lambda_{1,1} = \lambda_{2,1}$ as used in [17]. Such a constraint is however not suited to accurately characterize each fascicle independently. In [44,52], the fractions of occupancy were merged together. This, however, does not adequately represent the signal arising from each fascicle in presence of partial volume effect, and does not allow the computation of a full diffusion tensor associated with each white matter fascicle. Only the use of multiple non-zero b-values is a satisfying solution to disambiguate the estimation of the tensors and the fractions, and to enable characterization of each individual fascicle and of the unrestricted water component.

Our solution lies in a novel multi-fascicle estimation framework, CUSP-MFM, which is the combination of a novel multi-tensor estimation algorithm and an optimal acquisition scheme which satisfies the need of multiple non-zero b-values. The characteristics of our multi-tensor estimation procedure were driven by the objective to make it possible to represent multiple fascicles in clinical DWI with a relatively short acquisition time, compatible with pediatric and adult imaging. The *Maximum A Posteriori* formulation we employed enabled us to perform accurate and reliable multi-fascicle model estimation. Our model includes the estimation of an isotropic tensor which represents the free population of water molecules that is not affected by fiber structure barriers [42,43,45]. In this work we qualitatively did not observe a dramatic impact of adding this parameter when using a single-shell HARDI (Fig 10a and Fig 10c). In this case, there is no unique solution to the estimation due to the collinearity of the parameters, and the part of the DW signal coming from the free water population is incorporated in the tensor magnitude and in the fractions. In contrast, with multiple non-zero b-values (CUSP), the tensor magnitude and the fractions are not collinear anymore. We showed that the attempt to fit a model without the isotropic water compartment, *i.e.* a model that poorly represents the signal, perturbs the whole tensor estimation (Fig 10d). Therefore, to ensure reliable estimates, both multiple non-zero b-values and a model that accounts for the unrestricted water diffusion are necessary.

We show that when using an optimized acquisition scheme and when estimating the diffusion of unrestricted water, we can accurately estimate the fascicle orientation from the hindered

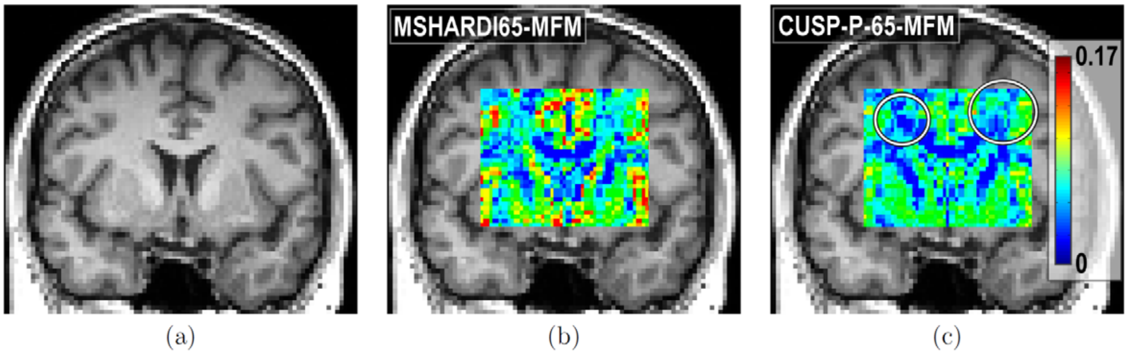

Figure 14. Comparison of CUSP and multi-shell HARDI via residual bootstrapping. (a) T1-weighted image showing the anatomy. (b) Standard deviation of the maximum FA when using MSHARDI-65-MFM. (c) Standard deviation of the maximum FA when using CUSP-65-MFM. The standard deviation of the maximum FA is significantly lower when using CUSP, showing a lower uncertainty in the MFM estimates.
doi:10.1371/journal.pone.0048232.g014

diffusion. In this work, we have relied on the assumption that, *for each fascicle*, the DW signal mono-exponentially decays with increasing b-value. Based on non-monoexponential decays measurements in voxels, other authors have suggested that a non-monoexponential model may be more appropriate [55,58–60], even for relatively low b-values [60]. However, these approaches have ignored the fascicle orientation heterogeneity ($N_f = 1$) and the CSF contamination when considering a model with non-monoexponential decay. In this case, the source of the non-monoexponential decay remains unclear. As illustrated in Fig. 2, mixing of monoexponential decays as modeled in our approach does lead to a non-monoexponential behavior in voxels. As established by [16], when the gradient strength is limited and when the DW signal is properly modeled by taking into account both the fascicle orientation heterogeneity ($N_f > 1$) and the CSF contamination, a monoexponential decay for the signal arising from *each* fascicle can be safely assumed. In contrast, if the diffusion signal of a single fascicle exhibits a non-monoexponential decay, then our current multi-fascicle model cannot fully represent it and a generalization of our model may be necessary. Other per-fascicle models could be easily introduced in our framework and will be investigated in future work.

We have formulated our multi-tensor estimation approach in the log-Euclidean framework [65] which is an elegant way to guarantee that each tensor matrix is symmetric positive definite during the fitting. Other authors have considered a Cholesky parameterization of the diffusion tensor [79], or Bayesian approaches with priors on the eigenvalues [42,45] to ensure valid tensors. With the log-Euclidean framework, all computations are performed within the appropriate manifold, ensuring valid tensors at each step. To our knowledge the log-Euclidean framework has never been employed for multi-fascicle models. Not only does it ensure non-degenerate tensors, it also provides us with a metric to compare and regularize tensors. All of the information carried by tensors is taken into account with the log-Euclidean metric, and not only features extracted from the tensors. Importantly, tensor determinants in this framework are monotonically interpolated. It prevents the regularized tensors from experiencing the *swelling* effect which has been observed in both the Euclidean and Cholesky frameworks [64,65]. The swelling effect makes the estimated tensors larger than they should be. It particularly affects tensors at tissue borders such as the cerebrospinal fluid/white matter interface, where neighboring tensors are very dissimilar. Based on Monte Carlo experiments [80], have however suggested that an affine-invariant metric such as the log-Euclidean metric might lead to a larger bias in the case of extreme ADC values (either low or high). However, for the major brain tissues [80], shows that this bias is not observed.

We proposed a log-Euclidean regularization scheme which is not the direct extension of the one-tensor regularization. We suggested a particular approximation of the spatial gradient for multi-tensor fields (Equation 6). It relates neighboring tensors which are part of the same fascicle. Consequently, only tensors which are part of the same fascicle are regularized together. Introducing this regularization strategy is possible because we consider each fascicle independently. It would be difficult to integrate in DSI, QBI, GDTI, or SD because these approaches consider the general shape of the diffusion profile and not individual fascicles.

In this work we propose an acquisition scheme designed to enable accurate assessment of multiple white matter fascicles. Our CUSP (CUbe and SPhere) imaging technique combines a single-shell HARDI with gradients in its enclosing cube. The single-shell HARDI provides a full spherical sampling with the optimal SNR and the optimal TE for the chosen nominal b-value. Any gradient in the enclosing cube of the single-shell HARDI can be acquired *without* modifying the TE by choosing the appropriate gradient strength. It corresponds to a *cube of constant TE*. It enables acquisition of b-values up to 3 times the nominal b-value *while* achieving the same low TE as a single-shell HARDI. Consequently, and in contrast to multi-shell HARDI, it does not increase the imaging time, does not increase the eddy current distortion and it maintains the DWI signal-to-noise ratio by maintaining $\exp(-TE/T2)$. We envisaged three different CUSP variants (Fig. 3). The first, CUSP-T, is a truncated multi-shell HARDI. It employs the portion of multiple shells with uniformly spaced radius contained in the cube of constant TE. The second, CUSP-xT, is a truncated multi-shell HARDI which employs portions of shells with exponentially spaced radius to counter-balance the exponentially decreasing SNR with increasing b-values, and to achieve an improve uniformity of SNR. Finally, CUSP-P is a projected multi-shell HARDI, built by projecting the gradients of an outer shell at $3b_{\mathrm{nominal}}$ onto the faces of the cube of constant TE to avoid any increase in TE. This provides a uniform angular resolution and a large number of different b-values.

Our evaluation shows clear evidence that the estimation of both the tensors and the fractions of occupancy are improved when using CUSP instead of a single shell acquisition (Fig. 4, 5, 8). Additionally, we observed a substantial improvement of the angular resolution when using CUSP instead of a single shell

(Fig. 6). From an algebraic point of view, only the tensor magnitude and the fractions are collinear with a single non-zero b-value. Introducing several non-zero b-values should not impact the tensor eigen vectors in a noise free model system. However, consistent with the literature [14,43,61], we observed that introducing higher b-values helps in differentiating the different compartments. Consequently, CUSP benefits are three-fold: First it solves the collinearity inherent to the multi-fascicle modeling with a single-shell HARDI. Second it enables imaging at higher b-values, which facilitates the estimation of the orientation of each fascicle [14]. Third, when compared to a conventional single-shell HARDI acquisition, it does not increase the acquisition time, does not increase the eddy current distortion and does not alter the signal-to-noise ratio.

The CUSP-MFM's performance was assessed via various experiments on both synthetic and in vivo data. We focused on short acquisitions suitable for routine clinical use, especially for pediatric MRI. The angular resolution is substantially superior to the state-of-the-art ball-and-stick model implemented in FSL (Fig. 6), while CUSP-MFM estimates the full tensor. This might be explained by the fact that the stick is an over-simplification which does not fully capture the true signal arising from a fascicle. Incorrect estimation of the tensor eigenvalues perturbs the estimation of the orientation because the optimization attempts at fully explaining the DW signal with an unrealistic model, leading to less accurate estimates. This also leads to the detection of multiple sticks in the body of the corpus callosum, which is a known single fascicle region (Fig. 10). In contrast, CUSP-MFM incorporates a more complex model for each fascicle and enables the assessment of individual fascicles characteristics in addition to the brain connectivity, by computing diffusion tensor parameter for each fascicle. The estimated diffusion parameters of two uniform synthetic crossing fascicles were shown to be almost uniform with CUSP-MFM (Fig. 8 and Fig. 9). It was verified on real acquisitions by simulating variations of the partial volume fractions for each tensor, by rotation of the diffusion-weighted images with various angles. We showed that with CUSP-MFM, the fractional anisotropy computed along a tract did not vary with the partial voluming effect nor the regularization, which was not the case when using a single-shell HARDI acquisition (Fig. 13). CUSP-MFM enables the full estimation of the multi-fascicle model, which enables characterization of the fascicles.

Fig. 5 showed that for small angles and in the absence of model order selection, the reconstruction error for the fractions of occupancy (fAAD) is significantly increased. Indeed, in the case where $\mathbf{D}_1 = \mathbf{D}_2$, we have: $f_1 e^{-b_k \mathbf{g}_k^T \mathbf{D}_1 \mathbf{g}_k} + f_2 e^{-b_k \mathbf{g}_k^T \mathbf{D}_1 \mathbf{g}_k} = (f_1 + f_2) e^{-b_k \mathbf{g}_k^T \mathbf{D}_1 \mathbf{g}_k} + 0$. It is not possible to estimate the fractions of occupancy f_1 and f_2 because of a collinearity in the parameters. The DW signal can be explained either with two compartments with non-null fractions f_1 and f_2 or with a single compartment with fraction $(f_1 + f_2)$. This case ($\mathbf{D}_1 \approx \mathbf{D}_2$), however, can be easily detected and handled with model order selection.

The qualitative evaluation on real data (Fig. 10, 11 and 12) showed that the estimated tensors orientation matches the expected underlying anatomy. The estimation without model order selection (Fig. 10, 11) showed that CUSP-MFM recovers the fascicle orientations better than the ball-and-stick model in regions of a single fascicle, either with $N_f = 2$ or $N_f = 3$. Importantly, the estimation of $N_f = 3$ fascicles with only 35 DW-images were consistent with the anatomy (Fig. 11). We also observed that in contrast to HARDI-MFM, CUSP-MFM enables correct estimation of the isotropic water fraction in the CSF (Fig. 10, 11).

Finally, we demonstrated that the estimation uncertainty is higher when using a multi-shell HARDI instead of CUSP (Fig. 14). This is due to the larger minimum achievable TE when imaging the full multi-shell HARDI, leading to an acquisition with exponentially decreased SNR (see Eq 1 and Fig. 1).

Future work

Future work will focus on assessing different gradient schemes for the CUSP acquisition. Particularly, we will investigate the optimal ordering of the gradient directions. CUSP-MFM performance will be compared to Q-Ball Imaging and Spherical Deconvolution approaches for the assessment of connectivity.

Robust estimation will be also explored. It enables to reduce the influence of large residuals, making the estimation less sensitive to outliers than when using the least square criteria. It may provide a better robustness to patient motion and will be of particular interest for pediatric imaging.

Conclusions

We demonstrated and experimentally verified that multiple non-zero b-values are required to fully estimate multi-tensor models. As a solution we proposed CUSP-MFM which combines an optimal CUbe and SPhere (CUSP) acquisition technique with a novel algorithm for the estimation of the parameters of a Multi-Fascicle Model (MFM). Our proposed CUSP acquisition technique provides multiple high b-values with the optimal achievable TE. It does not increase the imaging time nor the eddy current distortion compared to a single-shell HARDI. Additionally, it does provide the optimal signal-to-noise ratio, leading to estimates with higher certainty. Our novel multi-fascicle fitting algorithm MFM is formulated as a *Maximum A Posteriori* estimation problem. It integrates an isotropic compartment, constrained estimation and an original regularization scheme in which only the tensors that are part of the same tract are regularized together. It ensures non-degenerate tensors and robust-to-noise estimates. Our evaluation shows that CUSP-MFM enables the representation of multiple white matter fascicles from a short duration acquisition. It enables characterization of each fascicle, in addition to the brain connectivity, which is of great interest for clinical applications. CUSP-MFM may enable new investigations of the white matter development and degeneration in research and in clinical practice.

CUSP Gradient Encoding Scheme

We provide the CUSP65 gradient encoding schemes in the Siemens format. On a Siemens scanner, this requires to set the imaged b-value to $b = 3000 \mathrm{s/mm}^2$ which corresponds to the b-value of the gradient of higher norm in the table. With this choice, the resulting minimum achievable TE correctly matches the minimum achievable TE of a single-shell HARDI at $b = 1000 \mathrm{s/mm}^2$.

```
[directions = 65]
CoordinateSystem = xyz
Normalisation = none
Vector[0] = (0, 0, 0)
Vector[1] = (0, 0, 0)
Vector[2] = (0, 0, 0)
Vector[3] = (0, 0, 0)
Vector[4] = (0, 0, 0)
Vector[5] = (1.00000, 0.00000, 0.00000)
Vector[6] = (0.16600, 0.98600, 0.00000)
Vector[7] = (0.11000, −0.66400, −0.74000)
Vector[8] = (0.90100, −0.41900, −0.11000)
Vector[9] = (0.16900, 0.60100, −0.78100)
Vector[10] = (0.81500, 0.38600, −0.43300)
Vector[11] = (−0.65600, −0.36600, −0.66000)
```

$\text{Vector}[12] = (-0.58200,\ -0.80000,\ -0.14300)$
$\text{Vector}[13] = (-0.90000,\ -0.25900,\ -0.35000)$
$\text{Vector}[14] = (-0.69300,\ 0.69800,\ \text{-0.17800})$
$\text{Vector}[15] = (0.35700,\ -0.92400,\ -0.14000)$
$\text{Vector}[16] = (0.54300,\ -0.48800,\ -0.68300)$
$\text{Vector}[17] = (0.52500,\ 0.39600,\ -0.75300)$
$\text{Vector}[18] = (0.63900,\ -0.68900,\ -0.34100)$
$\text{Vector}[19] = (-0.33000,\ -0.01300,\ -0.94400)$
$\text{Vector}[20] = (0.52400,\ 0.78300,\ -0.33500)$
$\text{Vector}[21] = (0.60900,\ -0.06500,\ -0.79100)$
$\text{Vector}[22] = (0.22000,\ -0.23300,\ -0.94700)$
$\text{Vector}[23] = (-0.00400,\ -0.91000,\ -0.41500)$
$\text{Vector}[24] = (-0.51100,\ 0.62700,\ -0.58900)$
$\text{Vector}[25] = (-0.41400,\ -0.73700,\ -0.53500)$
$\text{Vector}[26] = (-0.67900,\ 0.13900,\ -0.72100)$
$\text{Vector}[27] = (-0.88400,\ 0.29600,\ -0.36200)$
$\text{Vector}[28] = (-0.26200,\ -0.43200,\ -0.86300)$
$\text{Vector}[29] = (0.08800,\ 0.18500,\ -0.97900)$
$\text{Vector}[30] = (-0.29400,\ 0.90700,\ -0.30200)$
$\text{Vector}[31] = (0.88700,\ -0.08900,\ -0.45300)$
$\text{Vector}[32] = (-0.25700,\ 0.44300,\ -0.85900)$
$\text{Vector}[33] = (0.08600,\ 0.86700,\ -0.49100)$
$\text{Vector}[34] = (0.86300,\ 0.50400,\ -0.02500)$
$\text{Vector}[35] = (-1.00000,\ -1.00000,\ -1.00000)$
$\text{Vector}[36] = (1.00000,\ -1.00000,\ -1.00000)$
$\text{Vector}[37] = (-1.00000,\ 1.00000,\ -1.00000)$
$\text{Vector}[38] = (1.00000,\ 1.00000,\ -1.00000)$
$\text{Vector}[39] = (1.00000,\ 1.00000,\ 0.00000)$
$\text{Vector}[40] = (-0.00000,\ -1.00000,\ -1.00000)$
$\text{Vector}[41] = (-1.00000,\ -0.00000,\ -1.00000)$
$\text{Vector}[42] = (-1.00000,\ 1.00000,\ 0.00000)$
$\text{Vector}[43] = (-0.00000,\ 1.00000,\ -1.00000)$
$\text{Vector}[44] = (1.00000,\ -0.00000,\ -1.00000)$
$\text{Vector}[45] = (1.00000,\ -0.11968,\ -0.22826)$
$\text{Vector}[46] = (0.45391,\ 1.00000,\ -0.74490)$
$\text{Vector}[47] = (0.30929,\ -0.52908,\ -1.00000)$
$\text{Vector}[48] = (1.00000,\ 0.32570,\ -0.82547)$
$\text{Vector}[49] = (-0.53649,\ -0.28378,\ -1.00000)$
$\text{Vector}[50] = (1.00000,\ 0.28277,\ -0.16662)$
$\text{Vector}[51] = (0.37769,\ 0.13072,\ -1.00000)$
$\text{Vector}[52] = (-0.18512,\ 0.21731,\ -1.00000)$
$\text{Vector}[53] = (-0.32054,\ -1.00000,\ -0.32795)$
$\text{Vector}[54] = (0.37433,\ 1.00000,\ -0.18999)$
$\text{Vector}[55] = (-1.00000,\ 0.49160,\ -0.79472)$
$\text{Vector}[56] = (-0.09712,\ 1.00000,\ -0.03398)$
$\text{Vector}[57] = (-1.00000,\ -0.00905,\ -0.41514)$
$\text{Vector}[58] = (0.36282,\ -1.00000,\ -0.54229)$
$\text{Vector}[59] = (-0.52123,\ 1.00000,\ -0.11772)$
$\text{Vector}[60] = (-0.31196,\ 1.00000,\ -0.73018)$
$\text{Vector}[61] = (-1.00000,\ -0.69636,\ -0.40808)$
$\text{Vector}[62] = (-1.00000,\ 0.32257,\ -0.12697)$
$\text{Vector}[63] = (1.00000,\ -0.48206,\ -0.55084)$
$\text{Vector}[64] = (-0.06116,\ -0.17609,\ -1.00000)$

Author Contributions

Conceived and designed the experiments: BS SKW. Performed the experiments: BS. Analyzed the data: BS. Contributed reagents/materials/analysis tools: BS SKW. Wrote the paper: BS SKW.

References

1. Wesbey GE, Moseley ME, Ehman RL (1984) Translational molecular self-diffusion in magnetic resonance imaging. II. measurement of the self-diffusion coefficient. Invest Radiol 19: 491–498.
2. Moseley ME, Cohen Y, Kucharczyk J, Mintorovitch J, Asgari HS, et al. (1990) Diffusion-weighted MR imaging of anisotropic water diffusion in cat central nervous system. Radiology 176: 439–445.
3. Norris DG (2001) The effects of microscopic tissue parameters on the diffusion weighted magnetic resonance imaging experiment. NMR Biomed 14: 77–93.
4. Minati L, Weglarz WP (2007) Physical foundations, models, and methods of diffusion magnetic resonance imaging of the brain: A review. Concepts Magn Reson 30A: 278–307.
5. Mulkern R, Haker S, Maier S (2009) On High b Diffusion Imaging in the Human Brain: Ruminations and Experimental Insights. Magn Reson Imaging 27: 1151–1162.
6. Basser PJ, Mattiello J, LeBihan D (1994) Estimation of the effective self-diffusion tensor from the NMR spin echo. J Magn Reson B 103: 247–254.
7. Stejskal EO, Tanner JE (1965) Spin diffusion measurements: Spin echoes in the presence of a time-dependent field gradient. The Journal of Chemical Physics 42: 288–292.
8. Le Bihan D (1991) Molecular diffusion nuclear magnetic resonance imaging. Magn Reson Q 7: 1–30.
9. Conturo TE, McKinstry RC, Akbudak E, Robinson BH (1996) Encoding of anisotropic diffusion with tetrahedral gradients: a general mathematical diffusion formalism and experimental results. Magn Reson Med 35: 399–412.
10. Jones DK, Horsfield MA, Simmons A (1999) Optimal strategies for measuring diffusion in anisotropic systems by magnetic resonance imaging. Magn Reson Med 42: 515–525.
11. Mattiello J, Basser PJ, Bihan DL (1994) Analytical Expressions for the b Matrix in NMR Diffusion Imaging and Spectroscopy. J Magn Reson 108: 131–141.
12. Jones DK (2004) The effect of gradient sampling schemes on measures derived from diffusion tensor MRI: a Monte Carlo study. Magn Reson Med 51: 807–815.
13. Jones DK, Basser PJ (2004) "Squashing peanuts and smashing pumpkins": how noise distorts diffusion-weighted MR data. Magn Reson Med 52: 979–993.
14. Yeh CH, Tournier JD, Cho KH, Lin CP, Calamante F, et al. (2010) The effect of finite diffusion gradient pulse duration on fibre orientation estimation in diffusion MRI. Neuroimage 51: 743–751.
15. Assaf Y, Basser PJ (2005) Composite hindered and restricted model of diffusion (CHARMED) MR imaging of the human brain. Neuroimage 27: 48–58.
16. Ozarslan E, Shepherd TM, Vemuri BC, Blackband SJ, Mareci TH (2006) Resolution of complex tissue microarchitecture using the diffusion orientation transform (DOT). Neuroimage 31: 1086–1103.
17. Caan MW, Khedoe HG, Poot DH, den Dekker AJ, Olabarriaga SD, et al. (2010) Estimation of diffusion properties in crossing fiber bundles. IEEE Trans Med Imaging 29: 1504–1515.
18. Kwong KK, McKinstry RC, Chien D, Crawley AP, Pearlman JD, et al. (1991) CSF-suppressed quantitative single-shot diffusion imaging. Magn Reson Med 21: 157–163.
19. Alexander AL, Hasan KM, Lazar M, Tsuruda JS, Parker DL (2001) Analysis of partial volume effects in diffusion-tensor MRI. Magn Reson Med 45: 770–780.
20. Wedeen VJ, Reese TG, Tuch DS, Weigel MR, Dou JG, et al. (2000) Mapping fiber orientation spectra in cerebral white matter with fourier-transform diffusion MRI. In: Proceedings of 8th Annual Meeting ISMRM, Denver. p. 82.
21. Wedeen VJ, Hagmann P, Tseng WY, Reese TG, Weisskoff RM (2005) Mapping complex tissue architecture with diffusion spectrum magnetic resonance imaging. Magn Reson Med 54: 1377–1386.
22. Qin W, Yu CS, Zhang F, Du XY, Jiang H, et al. (2009) Effects of echo time on diffusion quantification of brain white matter at 1.5 T and 3.0 T. Magn Reson Med 61: 755–60.
23. Reese TG, Heid O, Weisskoff RM, Wedeen VJ (2003) Reduction of eddy-current-induced distortion in diffusion MRI using a twice-refocused spin echo. Magn Reson Med 49: 177–182.
24. Jones DK (2011) Visualization of diffusion MR images, Oxford University Press, chapter Diffusion MRI: Theory, Methods and Applications.
25. Pierpaoli C, Jezzard P, Basser PJ, Barnett A, Di Chiro G (1996) Diffusion tensor MR imaging of the human brain. Radiology 201: 637–648.
26. Peled S, Whalen S, Jolesz FA, Golby AJ (2009) High b-value apparent diffusion-weighted images from CURVE-ball DTI. J Magn Reson Imaging 30: 243–248.
27. Tuch DS (2004) Q-ball imaging. Magn Reson Med 52: 1358–1372.
28. Descoteaux M, Angelino E, Fitzgibbons S, Deriche R (2007) Regularized, fast, and robust analytical Q-ball imaging. Magn Reson Med 58: 497–510.
29. Barnett A (2009) Theory of Q-ball imaging redux: Implications for fiber tracking. Magn Reson Med 62: 910–923.
30. Tristán-Vega A, Westin CF, Aja-Fernández S (2009) Estimation of fiber orientation probability density functions in high angular resolution diffusion imaging. NeuroImage 47: 638–650.
31. Aganj I, Lenglet C, Sapiro G, Yacoub E, Ugurbil K, et al. (2010) Reconstruction of the orientation distribution function in single- and multiple-shell q-ball imaging within constant solid angle. Magn Reson Med 64: 554–566.

32. Zhan W, Yang Y (2006) How accurately can the diffusion profiles indicate multiple fiber orientations? A study on general fiber crossings in diffusion MRI. J Magn Reson 183: 193–202.
33. Canales-Rodríguez EJ, Melie-García L, Iturria-Medina Y (2009) Mathematical description of q-space in spherical coordinates: exact Q-ball imaging. Magn Reson Med 61: 1350–1367.
34. Lori NF, Conturo TE, Le Bihan D (2003) Definition of displacement probability and diffusion time in q-space magnetic resonance measurements that use finite-duration diffusion-encoding gradients. J Magn Reson 165: 185–195.
35. Canales-Rodríguez EJ, Lin CP, Iturria-Medina Y, Yeh CH, Cho KH, et al. (2010) Diffusion orientation transform revisited. Neuroimage 49: 1326–1339.
36. Ozarslan E, Mareci TH (2003) Generalized diffusion tensor imaging and analytical relationships between diffusion tensor imaging and high angular resolution diffusion imaging. Magn Reson Med 50: 955–965.
37. Liu C, Bammer R, Acar B, Moseley ME (2004) Characterizing non-gaussian diffusion by using generalized diffusion tensors. Magn Reson Med 51: 924–937.
38. Frank LR (2002) Characterization of anisotropy in high angular resolution diffusion-weighted MRI. Magn Reson Med 47: 1083–1099.
39. Tournier JD, Calamante F, Gadian DG, Connelly A (2004) Direct estimation of the fiber orientation density function from diffusion-weighted MRI data using spherical deconvolution. Neuroimage 23: 1176–1185.
40. Jian B, Vemuri BC (2007) A unified computational framework for deconvolution to reconstruct multiple fibers from diffusion weighted MRI. IEEE Trans Med Imaging 26: 1464–1471.
41. Ozarslan E, Vemuri BC, Mareci TH (2005) Generalized scalar measures for diffusion MRI using trace, variance, and entropy. Magn Reson Med 53: 866–876.
42. Behrens TE, Woolrich MW, Jenkinson M, Johansen-Berg H, Nunes RG, et al. (2003) Characterization and propagation of uncertainty in diffusion-weighted MR imaging. Magn Reson Med 50: 1077–1088.
43. Hosey T, Williams G, Ansorge R (2005) Inference of multiple fiber orientations in high angular resolution diffusion imaging. Magn Reson Med 54: 1480–1489.
44. Kreher BW, Schneider JF, Mader I, Martin E, Hennig J, et al. (2005) Multitensor approach for analysis and tracking of complex fiber configurations. Magn Reson Med 54: 1216–1225.
45. Melie-García L, C-Rodríguez EJ, Alemán-Gómez Y, Lin CP, Iturria-Medina Y, et al. (2008) A Bayesian framework to identify principal intravoxel diffusion profiles based on diffusion-weighted MR imaging. Neuroimage 42: 750–770.
46. Metzler-Baddeley C, O'Sullivan MJ, Bells S, Pasternak O, Jones DK (2012) How and how not to correct for CSF-contamination in diffusion MRI. Neuroimage 59: 1394–1403.
47. Latour LL, Warach S (2002) Cerebral spinal fluid contamination of the measurement of the apparent diffusion coefficient of water in acute stroke. Magn Reson Med 48: 478–486.
48. Tuch DS, Reese TG, Wiegell MR, Makris N, Belliveau JW, et al. (2002) High angular resolution diffusion imaging reveals intravoxel white matter fiber heterogeneity. MRM 48: 577–582.
49. Peled S, Friman O, Jolesz F, Westin CF (2006) Geometrically constrained two-tensor model for crossing tracts in DWI. Magn Reson Imaging 24: 1263–1270.
50. Pasternak O, Assaf Y, Intrator N, Sochen N (2008) Variational multiple-tensor fitting of fiber-ambiguous diffusion-weighted magnetic resonance imaging voxels. Magn Reson Imaging 26: 1133–1144.
51. Sotiropoulos SN, Bai L, Morgan PS, Auer DP, Constantinescu CS, et al. (2008) A regularized two-tensor model fit to low angular resolution diffusion images using basis directions. J Magn Reson Imaging 28: 199–209.
52. Malcolm JG, Shenton ME, Rathi Y (2010) Filtered multi-tensor tractography. IEEE Trans on Medical Imaging 29: 1664–1675.
53. Mulkern R, Zengingonul H, Robertson R, Bogner P, Zou K, et al. (2000) Multi-component apparent diffusion coefficients in human brain: relationship to spin-lattice relaxation. Magn Reson Med 44: 292–300.
54. Sehy JV, Ackerman JJ, Neil JJ (2004) Evidence that both fast and slow water ADC components arise from intracellular space. Magn Reson Med 48: 765–770.
55. Bennett KM, Schmainda KM, (tong) RB, Rowe DB, Lu H, et al. (2003) Characterization of continuously distributed cortical water diffusion rates with a stretched-exponential model. Magn Reson Med 50: 727–734.
56. Yablonskiy DA, Bretthorst GL, Ackerman JJ (2003) Statistical model for diffusion attenuated MR signal. Magn Reson Med 50: 664–669.
57. Schwarcz A, Bogner P, Meric P, Correze JL, Berente Z, et al. (2004) The existence of biexponential signal decay in magnetic resonance diffusion-weighted imaging appears to be independent of compartmentalization. Magn Reson Med 51: 278–285.
58. Maier SE, Vajapeyam S, Mamata H, Westin CF, Jolesz FA, et al. (2004) Biexponential diffusion tensor analysis of human brain diffusion data. Magn Reson Med 51: 321–330.
59. Jensen JH, Helpern JA, Ramani A, Lu H, Kaczynski K (2005) Diffusional kurtosis imaging: the quantification of non-gaussian water diffusion by means of magnetic resonance imaging. Magn Reson Med 53: 1432–1440.
60. Cheung MM, Hui ES, Chan KC, Helpern JA, Qi L, et al. (2009) Does diffusion kurtosis imaging lead to better neural tissue characterization? A rodent brain maturation study. Neuroimage 45: 386–392.
61. Behrens TE, Berg HJ, Jbabdi S, Rushworth MF, Woolrich MW (2007) Probabilistic diffusion tractography with multiple fibre orientations: What can we gain? Neuroimage 34: 144–155.
62. Scherrer B, Warfield SK (2010) Why multiple b-values are required for multi-tensor models. Evaluation with a constrained log-Euclidean model. In: ISBI 2010: Proceedings of the 2010 IEEE international conference on Biomedical imaging. pp. 1389–1392.
63. Koay CG, Carew JD, Alexander AL, Basser PJ, Meyerand ME (2006) Investigation of anomalous estimates of tensor-derived quantities in diffusion tensor imaging. Magn Reson Med 55: 930–936.
64. Fillard P, Pennec X, Arsigny V, Ayache N (2007) Clinical DT-MRI estimation, smoothing, and fiber tracking with log-Euclidean metrics. IEEE Trans Med Imaging 26: 1472–1482.
65. Arsigny V, Fillard P, Pennec X, Ayache N (2006) Log-euclidean metrics for fast and simple calculus on diffusion tensors. Magn Reson Med 56: 411–421.
66. Powell MJD (2009) The BOBYQA algorithm for bound constrained optimization without derivatives. In: Technical report NA2009/06. Department of Applied Mathematics and Theoretical Physics, Cambridge England.
67. Scherrer B, Warfield SK (2011) Toward an accurate multi-fiber assessment strategy for clinical practice. In: ISBI 2011: Proceedings of the 2011 IEEE international conference on Biomedical imaging. pp. 2140–2143.
68. Conturo TE, McKinstry RC, Aronovitz JA, Neil JJ (1995) Diffusion MRI: precision, accuracy and flow effects. NMR Biomed 8: 307–332.
69. Neil J, Miller J, Mukherjee P, Hüppi PS (2002) Diffusion tensor imaging of normal and injured developing human brain - a technical review. NMR Biomed 15: 543–552.
70. Cook PA, Symms M, Boulby PA, Alexander DC (2007) Optimal acquisition orders of diffusion-weighted MRI measurements. J Magn Reson Imaging 25: 1051–1058.
71. Besag J (1986) On the statistical analysis of dirty pictures. J Roy Statist Soc Ser B 48: 259–302.
72. Alexander DC, Barker GJ, Arridge SR (2002) Detection and modeling of non-gaussian apparent diffusion coefficient profiles in human brain data. Magn Reson Med 48: 331–340.
73. Ruiz-Alzola J, Westin CF, Warfield SK, Alberola C, Maier S, et al. (2002) Nonrigid registration of 3D tensor medical data. Med Image Anal 6: 143–161.
74. Tristán-Vega A, Aja-Fernández S (2010) DWI filtering using joint information for DTI and HARDI. Med Image Anal 14: 205–218.
75. Chung S, Lu Y, Henry RG (2006) Comparison of bootstrap approaches for estimation of uncertainties of DTI parameters. Neuroimage 33: 531–541.
76. Whitcher B, Tuch DS, Wisco JJ, Sorensen AG, Wang L (2008) Using the wild bootstrap to quantify uncertainty in diffusion tensor imaging. Hum Brain Mapp 29: 346–362.
77. Raffelt D, Tournier JD, Rose S, Ridgway GR, Henderson R, et al. (2012) Apparent Fibre Density: a novel measure for the analysis of diffusion-weighted magnetic resonance images. Neuroimage 59: 3976–3994.
78. Aurobrata G, Rachid D (2011) Extracting geometrical features & peak fractional anisotropy from the ODF for white matter characterization. In: ISBI 2011: Proceedings of the 2011 IEEE international conference on Biomedical imaging. pp. 266–271.
79. Wang Z, Vemuri BC, Chen Y, Mareci TH (2004) A constrained variational principle for direct estimation and smoothing of the diffusion tensor field from complex DWI. IEEE Trans Med Imaging 23: 930–939.
80. Pasternak O, Sochen N, Basser PJ (2010) The effect of metric selection on the analysis of diffusion tensor MRI data. Neuroimage 49: 2190–2204.